

3D Surface Reconstruction
and
2D Segmentation of
Scanning Electron Microscopy Images

3D Surface Reconstruction
and
2D Segmentation of
Scanning Electron Microscopy Images

By
Yasamin Sartipi

A Thesis
Submitted to the School of Graduate Studies
in Partial Fulfillment of the Requirements
for the Degree
Master of Science

McMaster University
© Copyright by Yasamin Sartipi, April 25, 2019

MASTER OF SCIENCE(2019)
COMPUTER SCIENCE

McMaster University
Hamilton, Ontario

TITLE: 3D surface reconstruction and 2D segmentation of Scanning Electron Microscopy images

AUTHOR: Yasamin Sartipi B.Eng. (Azad University Tehran), M.A.I. (Kharazmy University)

SUPERVISOR: Dr. Christopher K. Anand & Dr. Nabil Bassim

NUMBER OF PAGES: xii, 49

LEGAL DISCLAIMER: This is an academic research report. I, my supervisor, defence committee, and university, make no claim as to the fitness for any purpose, and accept no direct or indirect liability for the use of algorithms, findings, or recommendations in this thesis.

Abstract

Scanning Electron Microscopy (SEM) used in a wide range of industrial and research applications. SEM produces greyscale images of a specimen by bombarding it with high-energy electrons, causing secondary and backscattered electrons and x-ray photons to be produced by several different mechanisms. Images obtained from SEM have information about the topography and composition of the sample. Because the electron beam must scan the sample in a serial, rostered fashion, SEM imaging is time consuming and expensive. In this thesis we give two methods of using mathematical optimization to extract extra information from SEM images.

In the first part, we reconstruct three-dimensional images from two-dimensional SEM images acquired with different types of electron contrasts and in different orientations, reducing the need for costly Atomic Force Microscopy (AFM) probes or other 3-D metrology tools. In the second part, we accelerate the SEM process of imaging by reconstructing full images from images with only a fraction of the rows scanned, and apply this to the problem of segmenting images used in circuit analysis for reverse engineering. In the example images, we show that by simultaneously acquiring two images from different types of electron detectors, and skipping three out of four scan lines, we can segment the example images with partial images acquired in one quarter of the time. To use two sparse, simultaneously-acquired images to build the segmentation model, we construct a second optimization problem which optimally combines the two images taking into account the different signal and noise characteristics of the two images.

Acknowledgments

First and foremost, I would like to thank Dr. Christopher Anand and Dr. Nabil Bassim for their continuous support, their patience, motivation, and immense knowledge. Their guidance helped me in every stage of research and writing of this thesis. I could not have imagined having better advisors and mentors in my master's study. Also I want to thank many people at TechInsights for describing the 2D segmentation problem and providing the data for us, and at Fibics, Inc for sharing their expertise about electron detectors. My sincere thanks also goes to the many research scientists at the Canadian Centre for Electron Microscopy for providing their help and expertise. I sincerely thank Christopher Schankula, Aidan Ross, Weiwei Zhang, Hesham El-Sherif, Khatereh Maleki and Sam Norris for your help. Finally I want to thank my parents Dr. Azadeh Nazari and Mehdi Sartipi and my love Amid for their encouragement, support and love.

Contents

Appendices	i
Abstract	iii
Acknowledgments	v
List of Figures	ix
List of Notation	xi
1 Introduction	1
2 Background	3
2.1 What is Scanning Electron Microscopy?	3
2.1.1 How SEM works?	3
2.1.2 Electron-Sample Interactions	4
2.1.3 SEM Imaging Parameters	8
2.1.4 Electron Detectors	8
2.1.5 Contrast	10
2.2 Optimization	12
2.2.1 Optimization Tools	14
3 3D Reconstruction	17
Abstract	17
3.1 Introduction	17
3.2 Theory	19
3.2.1 Linear Model (LM-BSE)	21
3.2.2 Quadratic Model (QM-BSE)	22
3.2.3 Adding SE Mode Information	22
3.3 Methods	28
3.4 Results	28
3.5 Discussion	30
3.5.1 Future Work	31
3.6 Acknowledgments	32
4 Segmentation of SEM Images for Reverse Engineering	33

Abstract	33
4.1 Introduction	33
4.2 Semiconductor Circuits	34
4.2.1 Data	34
4.3 Methods	35
4.4 Results	41
4.5 Discussion	43
4.6 Acknowledgments	44
5 Conclusion	45

List of Figures

2.1	The FEI Magellan 400, a high-resolution SEM.	4
2.2	Schematic of the different types of electron-sample interactions that occur in a sample as a function of depth.	5
2.3	Schematic of the electron-nucleus interaction present in BSE generation. . .	6
2.4	Schematic of SE generation mechanism by electron-electron interactions. . .	7
2.5	Different types of SE generated in the SEM chamber.	8
2.6	Schematic of Everhart - Thornley detector showing the scintillator with a thin metallic surface electrode (blue) with an applied bias of positive 10 kV surrounded by an electrically isolated Faraday cage	9
2.7	Through-lens detector showing that BSE still escape into the sample chamber while all SEs are collected in detectors located in the electron column. . . .	10
2.8	Compositional contrast from BSE contrast.	11
2.9	<i>Left:</i> BSE image of a zinc sample coated steel sheet. <i>Right:</i> SE image of the same area of the sample.	12
2.10	Edge effect on a tin sphere specimen.	13
2.11	<i>Left:</i> a greyscale image part of an electronic circuit. <i>Right:</i> Red line is the image histogram with two greyscale values. Green and the blue line are two normal distribution that are minimized with the histogram by the optimization problem	14
3.1	This method uses eight BSE images taken from different angles by rotating the sample stage (<i>top left</i>); and the sum of SE images taken at the same angles (<i>top-right upper</i>). In the first problem, the squares of the opposite BSE images are subtracted (<i>middle</i>), and these values are compared in the optimization problem to differences in the heightmap ($h_{i,j}$, <i>top-right lower</i>) of the appropriate neighbouring pixels. The calculation of each absolute value requires a parameter $(\theta, \alpha, \gamma, \omega)$ (<i>bottom</i>).	20
3.2	<i>Top:</i> Sum of eight SE images; <i>middle:</i> definition of variables; <i>bottom:</i> profile plot of yellow line on the SE image, with best-fit even quartic $y = 25.753x^4 + 3.89x^2 + 22.487$	23
3.3	Four discrete gradient approximations.	24
3.4	<i>Top:</i> Numerical errors caused by a fixed gradient discretization, $G_{0,i,j}$. <i>Bottom:</i> $G_{k_{i,j},i,j}$ the minimizing case.	25
3.5	<i>Left:</i> Result of integrating $I_0^2 - I_{180}^2$ along the x-axis. <i>Right:</i> Result of solving LM-BSE.	29

3.6	SE information produces rotationally symmetric and rounder ball. <i>Top</i> : two views of the heightmap h^b produced by the first linear model. <i>Bottom</i> : two views of the heightmap h produced by the second linear model which uses the direction of ∇h^b and the SE images.	29
3.7	Validation of the method on silicon test objects: McMaster Fireball, towers and trenches. The columns show sample BSE and SE images, the AFM heightmap, a 3D rendering of the AFM heightmap, the optimized heightmap, h^b and a 3D rendering thereof. Of note are the the limitations of the AFM to probe the narrow trenches in the top sample, the accuracy of h^b in representing the trenches surrounding the test towers and the edge of the cut region, in agreement with the AFM probe, in the middle sample.	30
3.8	<i>Left</i> : One of eight ETD-BSE-mode images of sputtered tin balls. <i>Right</i> : Optimized heightmap h^b , in which most of the smaller balls are missing.	31
4.1	<i>Top</i> : Segmentation via thresholding. <i>Bottom</i> : Thresholding after filtering with a Gaussian filter.	35
4.2	Backscattered SEM image and identification of regions for segmentation using Canny Edge detection.	36
4.3	Caption for LOF	37
4.4	<i>Left</i> : BSE Detector <i>Right</i> : InLens detector SE images of metallization lines	38
4.5	Partial BSD and InLens images, showing every fourth scan line.	38
4.6	Weights of Neighbours.	39
4.7	<i>Left</i> : Results of the first step using only the BSE image, <i>Right</i> : Results of the first step using only the Inlens image.	39
4.8	<i>Left</i> : Sample noise. <i>Middle</i> : FFT of a line of noise. <i>Right</i> : Empirical point-spread function for noise.	40
4.9	minimums in the polynomial.	40
4.10	<i>Left</i> : First step result reconstructed from one fourth of the scan lines, <i>Right</i> : Second step result with $b=0$, $d=1$, $v=2$, $\lambda_1=40000$, $\lambda_2=100000$	42
4.11	<i>Left</i> : BSD image, <i>Middle</i> : two partial images from BSD and InLens detectors with one quarter of the lines. <i>Right</i> : First step result.	42
4.12	Second step results with quarter of scanning lines, and different choices of parameters.	43
4.13	<i>Left</i> : BSD image, <i>Middle</i> : two partial images from BSD and InLens detectors with half of the lines. <i>Right</i> : First step result.	43
4.14	Second step results with half the scan lines, and different choices of parameters.	44

List of Notation

Symbol	Description
θ	the tilt angle of the stage
ϕ	angle between the surface normal and detector
η	distribution of BSEs leaving the surface of the specimen
δ	distribution of SEs leaving the surface of the specimen
d_p	the diameter of the final beam on the surface of the sample
i_p	current in the electron beam reaching the object surface and generating imaging signals
α_p	the half-angle of the cone of the electrons converging onto the specimen
V_0	accelerating voltage of the electron gun
μ	mean
σ	standard deviation
$p_{\mu,\sigma}(k)$	normal distribution of pixel k
$q(k)$	frequency of pixel k
I_x	BSE image taking by rotation of $x \in \{0^\circ, 45^\circ, 90^\circ, 135^\circ, 180^\circ, 225^\circ, 270^\circ, 315^\circ\}$
$h(x,y)$	height of the sample on the usual coordinates
$h_{i,j}^p$	output heightmap in BSE linear and quadratic model indexed by the pixel location (i, j)
I_{SE}	sum of SE images taken from $\{0, 45, 90, 135, 180, 225, 270, 315\}$ angles
$\theta_{i,j}$	variable to encode absolute values in optimization problem
$\alpha_{i,j}$	variable to encode absolute values in optimization problem
$\gamma_{i,j}$	variable to encode absolute values in optimization problem
$\omega_{i,j}$	variable to encode absolute values in optimization problem
$\beta_{i,j}$	variable to encode absolute values in optimization problem
$\sigma_{i,j}$	variable to encode absolute values in optimization problem for regularization
λ	Penalty or regularization parameter
r	the radius of a sphere
s	slope
$y_{i,j}$	intermediate value used to calculate slope
$x_{i,j}$	equivalent radius for each pixel
$G_{i,j}$	gradient approximations
$G_{k_{i,j},i,j}$	minimum gradient approximations
$k_{i,j}$	minimal-length case of gradient
$G_{\uparrow,i,j}$	vertical component of the Gradient
$G_{\leftrightarrow,i,j}$	horizontal component of the Gradient
$G'_{\leftrightarrow,i,j}$	result of gaussian filter applied on $G_{\leftrightarrow,i,j}$
$G'_{\uparrow,i,j}$	result of gaussian filter applied on $G_{\uparrow,i,j}$
$H_{\uparrow,i,j}$	expected vertical component of the gradient

Symbol	Description
$H_{\leftrightarrow,i,j}$	expected horizontal component of the gradient
\tilde{G}	normalized of G'
w	weighting factor in BSE+SE model
$V_{i,j}$	the pixel of the reconstructed image at position (i, j)
I_{BSD}	image by BSD detector
I_{InLens}	image by InLens detector
\tilde{B}_k	reconstructed vector of noise
S	subset of pixels acquired
b	grey scale value
d	grey scale value
v	grey scale value
λ_1	penalty parameter
λ_2	penalty parameter
w	2d array of weights for neighbourhood comparisons
$\tilde{\zeta}(x)$	impulse with exponential decay

Chapter 1

Introduction

In this thesis we apply mathematical optimization to Scanning Electron Microscope (SEM) image processing. Electron microscopes produce greyscale images by scanning an electron beam across the surface of a specimen, and measuring the number of electrons which return from the sample via several physical mechanisms and are resolved at different energies. SEMs generate 2D greyscale images of different contrasts depending on the detector used and the settings of the microscope. The electron beam forms different signals that give us information about composition and surface topography of the sample. In Chapter 2 we explain the physics of SEM image formation, how it is modelled mathematically, and how optimization problems related to extracting additional information are specified, with an example relevant to this thesis.

In Chapter 3 we present a method to produce three dimensional heightmaps (i.e., topography) from multiple 2D SEM images with Backscatter Electron (BSE) and Secondary Electron (SE) contrasts. In this chapter the images for image reconstruction are acquired after rotating the sample in the microscope sample stage, which is equivalent to placing multiple detectors in the SEM. The resulting heightmap estimates are compared for accuracy against Atomic Force Microscopy (AFM) heightmaps.

The process of mapping the surface of a sample using electronic microscopy is expensive and time consuming. There are different solutions in order to speed image acquisition such as collecting partial images by skipping scan lines, and fusing noisy images from multiple detectors. In Chapter 4 we present an optimization method for producing segmented images from partial image data. The method uses two optimization problems: one to complete the partial images, and a second one, which uses the first solution as an initial guess, in order to produce segmented images.

In the last chapter, we discuss the common features of the optimization problems, their results, and suggested future work.

This thesis contain two papers (as of current writing) submitted for publication in a journal. The first paper which is included as Chapter 3 is a group work. Aidan Ross, Weiwei Zhang, Samuel Norris, Hesham El-Sherif are co-authors of this paper under supervision of Dr. Christopher Anand and Dr. Nabil Bassim.

Aidan Ross and I worked on the optimization models together. I implemented the linear model and Aidan Ross implemented the non-linear model. The examples in the paper/Chapter 3 were computed using the linear model I developed. Weiwei Zhang and I collected images on the SEM. Samuel Norris used Focused Ion Beam-SEM to fabricate

silicon test samples and Hesham El-Sherif performed the AFM tests and helped me to analyze the test results. All other work is mine. The second paper (Chapter 4) presents my work.

Chapter 2

Background

2.1 What is Scanning Electron Microscopy?

SEM provides us surface visualization and characterization of organic and inorganic specimens on the length scale of nanometers to micrometers. With SEM we can get topographic and compositional information. Due to the fact that SEM images have high resolutions, they play a vital role in the examination and analysis of microstructure. Since SEMs have large depth of field they can be used to image specimens with non-flat surfaces. Furthermore SEM is able to examine objects at a wide range of magnifications (pixel sizes from 1nm to $2\mu m$).

2.1.1 How SEM works?

SEM has three major components, the electron column, the specimen chamber, and the control console. See Figure 2.1. The essential components of the electron column are the electron gun which emits high energy electrons that travel down the column passing through some lenses which focus the beam on the sample located on the stage in the chamber. Deflection coils control the beam raster across the specimen, while the objective lens defines the focus of the electron beam. SEMs have different kinds of detectors which count electrons returning from the sample. By scanning the electron beam across the sample, the primary beam interacts with the sample and secondary signals are generated and collected. Based on their interaction at the electron detectors, we obtain a certain level of output signal current, which corresponds to a contrast level at that spot. The beam rasters and the signal is chopped into a series of pixels, which is a digitization of a continuous analogue signal. We can turn these greyscale values into an image. The control console contains a viewing screen and a computer control unit. The important microscope parameters we can control are beam energy, landing energy, beam current, convergence angle, working distance, and probe diameter, which we define below. The specimen chamber is held under vacuum and contains a sample stage to which the sample is affixed. The stage is capable of translation, rotation, and tilt to different orientations relative to the electron beam.



Figure 2.1: The FEI Magellan 400, a high-resolution SEM.

2.1.2 Electron-Sample Interactions

The energy of the electrons in the beam can be controlled by the acceleration voltage of the electron gun. When the electron beam hits the sample it penetrates into the sample to the depth of a few microns, with higher-energy electrons penetrating deeper. See Figure 2.2. This produces different signals such as backscatter electrons, secondary electrons, characteristic x-rays and other photons of various energies. These signals contain information about the electronic and chemical structure, including the atomic numbers of the sample's constituent atoms and sample's chemical and morphological arrangements. The most historically most widely-used signals for SEM imaging are backscatter and secondary electrons.

Backscattered electrons

When electrons in the beam go through the sample some electrons go close enough to the nucleus of an atom that they interact with the nuclear field of the atom, see Figure 2.3. The strength of that interaction causes the electron to “slingshot” around that atom, radically changing its electron trajectory without appreciably losing its energy. Following this interaction, the electron continues with a straight line trajectory until it encounters another atom or another interaction mechanism within the sample. If the electron reaches the surface of the sample and enters the sample chamber vacuum, it travels without interaction in the chamber until it hits the chamber wall or a backscattered electron detector. The number of these electrons hitting the detector tells us about the local chemical environment in the sample.

Elements with larger atomic number produce more BSE yield. Also BSE yield also

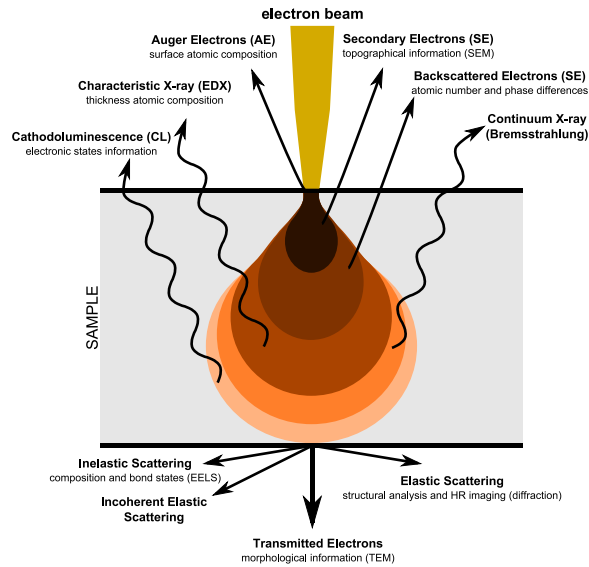


Figure 2.2: Schematic of the different types of electron-sample interactions that occur in a sample as a function of depth. ¹

¹ This image is licensed under the Creative Commons Attribution-Share Alike 4.0 International by user Rob Hurt.

depends on the beam energy. BSE yield is quantified by the BSE coefficient $\eta = N_{BSE}/N_B$ where N_B is the number of beam electrons that enter the specimen and N_{BSE} is the number of those electrons that we observe as backscattered electrons.

Dependence of BSE on angle of incidence

The tilt angle θ is the angle between the surface normal and the path of the electron beam. The number of BSEs increases with increasing tilt. This happens because the forward path after elastic scattering, while random, is biased to the forward direction, i.e., electrons tend to continue moving in the same direction after scattering as they were initially traveling. When $\theta = 0$, i.e., when the beam strikes perpendicular to the surface, not only do the electrons tend to travel further into the surface after scattering, but the location of the

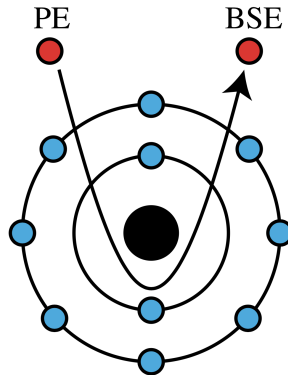


Figure 2.3: Schematic of the electron-nucleus interaction present in BSE generation. PE is a primary electron and BSE is the backscatter electron. ¹

¹ This image is licensed under Creative Commons Attribution-Share Alike 4.0 International by user Claudionico.

scattering tends to be deeper, so there is less likelihood they will emerge from the surface, and on to the detectors.

Dependence of BSE on Angle of Detector

The distribution of BSEs leaving the surface also depends on the angle, ϕ , between the surface normal and the detector. When the tilt is 0° there is a simple relationship between the signal strength and the angle ϕ ,

$$\eta(\phi) = \cos(\phi). \quad (2.1)$$

Secondary electrons

Secondary electrons are low-energy electrons that are generated by the interaction of the primary incident electron beam with the valence electrons of the atom, generating newly-released low-energy electrons. These low-energy electrons often recombine with the sample atoms, or are “absorbed”. While secondary electrons are generated everywhere relative to the incident and backscattered electrons, only the ones generated near the surface are released into the chamber vacuum, where they can be detected.

Unlike BSEs, the number of SEs is insensitive to the element atomic number. Also the number of SEs rises when the beam energy is lowered, because they are more likely to be absorbed into an electron shell. SEs have a typical energy of 1-6 eV. SE yield is quantified by the SE coefficient $\delta = N_{SE}/N_B$ where N_B is the number of beam electrons that enter the specimen and N_{SE} is the number of secondary electrons that are observed.

Secondary electrons come from near the surface. These electrons have information about the topography of the sample and are detected by an electron detector known as an

Everhart-Thornley detector, see Figure 2.4. They are called secondary electrons because they are new charged particles generated through electron-orbital electron process. They have much lower energy than backscatter electrons, and their paths after leaving the surface of the specimen are bent by electric fields.

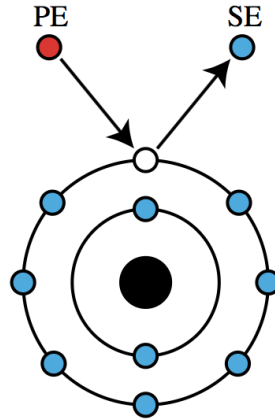


Figure 2.4: Schematic of SE generation mechanism by electron-electron interactions. PE is a primary electron and SE is the backscatter electron. ¹

¹ This image is licensed under the Creative Commons Attribution-Share Alike 4.0 International by user Rob Hurt.

Tilt dependence of SE

The number of SEs increase with increasing tilt angle, θ , the angle between the beam and the surface normal of the sample. By tilting the sample, the primary beam electrons travel in the near-surface region of the sample and fewer electrons penetrate to deeper regions. Consequently it is more likely that SEs will escape from the surface rather than being absorbed.

Angular distribution of SE

The angular distribution of SEs follows

$$\delta(\phi) = \frac{\delta_0}{\cos(\phi)} \quad (2.2)$$

where δ_0 is a constant, and ϕ is an angle between initial escape direction and the surface normal. Note that this effect is smaller than the dependence on θ , and we will not use it in this thesis.

SE Components: SE1, SE2, SE3, SE4

SEs can be interactions with the primary incident electron beam, in which case they are called SE1 electrons. But they can also be produced by backscatter electrons traveling

within the sample, producing SE2 electrons or hitting the column or chamber wall, producing SE3 electrons, as well as primary electrons hitting the column internally, producing SE4 electrons. See Figure 2.5. SE2, SE3 and SE4 degrade the resolution of the image because the signal emitted does not correspond to the position of the input probe electron but are still gathered by the Everheart-Thornley detector (see below) and contribute to noise in the image.

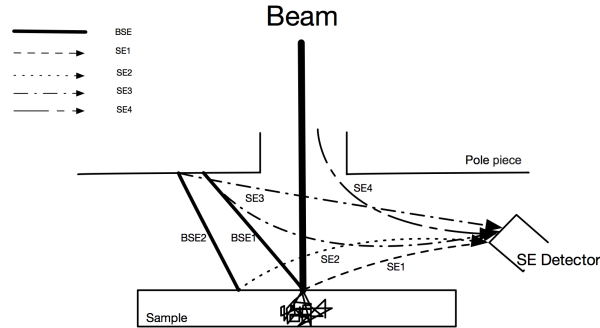


Figure 2.5: Different types of SE generated in the SEM chamber.

2.1.3 SEM Imaging Parameters

It is important to know the imaging conditions and parameters because it helps to analyze images correctly. Feature visibility and image sharpness are affected by four parameters: electron probe size d_p , the electron probe current i_p , the electron probe convergence angle (α_p) and the electron beam accelerating voltage $V_0(kV)$, where

1. d_p is the diameter of the final beam on the surface of the sample,
2. i_p is the current in the electron beam reaching the object surface and generating imaging signals,
3. α_p is the half-angle of the cone of the electrons converging onto the specimen, which effects the depth of focus, and
4. V_0 (kV) is the accelerating voltage of the electron gun, which effects the energy of the electrons.

2.1.4 Electron Detectors

Detectors collect and convert the signal of interest that leaves the specimen as a result of interaction with the electron beam. BSE and SE are two important signals for imaging. These two types of electrons have very different characteristics due to the generation mechanisms outlined above. They have different properties such as different energy levels, and different fractions of electron yield as a function of incident beam direction and directionality of emission. Each of these signals gives information about the sample.

The location of the the detector, its size, its efficiency in converting radiation into a useful signal and its bandwidth are four important characteristics of detectors.

Everhart-Thornley (E-T) Detector

This detector measures a combination of SE and BSEs and was invented by Everhart-Thornley in 1960. E-T detectors have a large solid angle of collection, high amplifier gain and low noise.

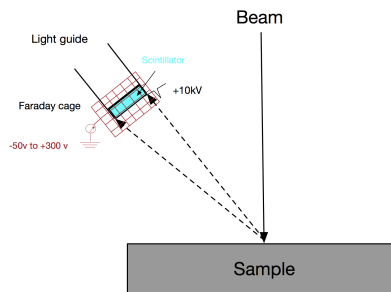


Figure 2.6: Schematic of Everhart - Thornley detector showing the scintillator with a thin metallic surface electrode (blue) with an applied bias of positive 10 kV surrounded by an electrically isolated Faraday cage

When an electron enters an E-T detector, it hits a scintillator, transforming its energy into a photon. The photon goes through a light pipe which is connected to a photomultiplier tube. In the photomultiplier, photons are converted into a current which is amplified by a preamplifier and an amplifier.

There is a Faraday cage around the E-T detector that can be biased and control whether SEs enter the detector. When its voltage is near zero or negative SE detection is stopped, because SEs are repelled by the Faraday cage field and only higher-energy BSEs are collected. When the Faraday cage potential has a large positive voltage, SEs are attracted and detected. Note that BSEs can travel into detectors as well so we see a combination of SE1, SE2, SE3 and BSEs on such images. BSEs typically do not lose much energy, and so have an accelerating voltage close to that of the incident electron beam (1-30 keV).

Through-the-Lens Detector (TTL)

Referring to Figure 2.7, Snorkel-type lenses are electromagnets coiled around the electron gun to produce a strong magnetic field parallel to the electron beam. SE1s and SE2s that are emitted from the sample are trapped and forced to spiral around this strong magnetic field, especially for short working distances (i.e., distance between the gun and the sample). SE1s and SE2s move in a spiral direction around the lines of magnetic flux up through the lens, to the end of the field where the detector is located. The actual detector could be an ET detector. Although TTL detectors are only sensitive to SE signals, the SE2 component is created from BSEs as they exit from the surface. Consequently, TTL is still sensitive to contrast effects arising from the BSE signal.

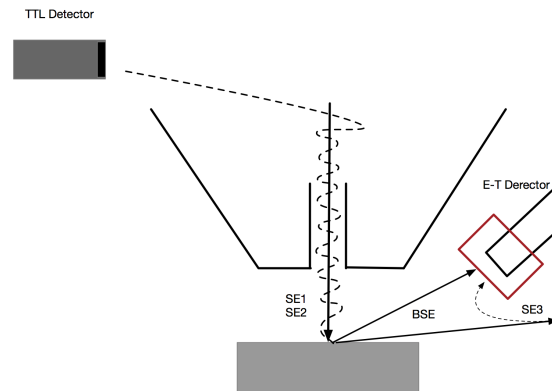


Figure 2.7: Through-lens detector showing that BSE still escape into the sample chamber while all SEs are collected in detectors located in the electron column.

Dedicated Backscattered Electron Detectors

BSEs contain information about the composition of the sample. One important class of detectors is solid-state diode detectors. This detector works on the principle of electron hole production induced in a semiconductor by energetic electrons.

An electron penetrates the detector and creates a series of electron/hole pairs in a p-n junction operated with reverse polarity. This allows a current to flow. The current is measured and a grey-scale pixel value is assigned based on the total current.

2.1.5 Contrast

Contrast is an important concept in SEM. It is a measure of real information in the signal. Contrast can be based on the properties of the specimen including as shape and elemental composition. We need to consider the detector and the sample as a complete system in discussing the contrast. The contrast we see is the result of both the signal generation in the sample and the electronic properties of the detectors which can be adjusted.

Contrast can be affected by characteristic of the beam—specimen interaction, properties of the specimen, the nature of the signal carrier and the properties of the detector such as position, size and the response of the detectors. Contrast is determined by three components:

1. Number component: The number of electrons leaving the specimen.
2. Trajectory component: contrast affected by the path the electron travels after leaving the specimen.

3. Energy component: The image intensity also depends on the energy of the detected electrons. The higher the atomic number, the higher the energy of the BSEs.

Compositional Contrast

Differences in the specimen's chemical composition create compositional contrast for backscatter electrons:

As shown in the Figure 2.8 (A) the sample is a flat, smooth block composed of one element. The contrast is the same trough the whole image because BSE, SE and all other signals would not change for the whole sample. Now consider two different kinds of elements in two different regions of the sample, Figure 2.8 (B). One of the element's atomic number is greater than the other ($Z_1 \leq Z_2$) so the number of backscatter electrons emitted from region two is more than the number of backscatter electrons emitted from region one. Also the number of secondary electrons emitted from two regions might be different but in a less predictable manner. Since the number of backscatter electrons emitted from heavier elements is greater, the heavier element would appear brighter than the other element in the greyscale image. As shown in Figure 2.9 on the left, we are able to observe different materials in different greyscale intensities. Since zinc is heavier than steel, more BSEs are emitted from its region, consequently it appears brighter. On the right we have an SE image of the same part of the sample. SEs come from the near-surface area so we can see the topography of the sample better. However the number of SEs does not tell us about composition of the sample.

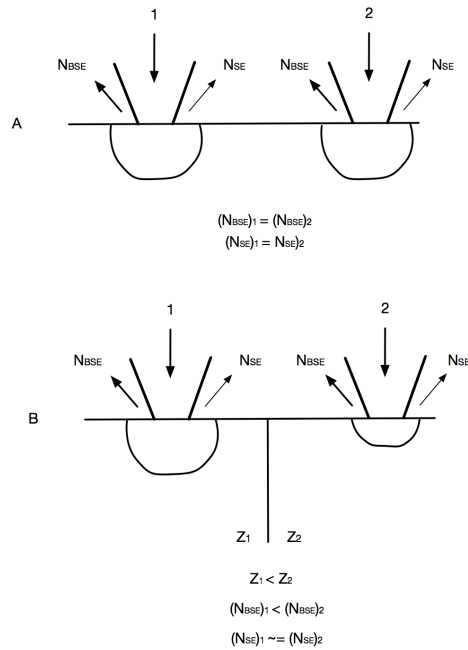


Figure 2.8: Compositional contrast from BSE contrast.

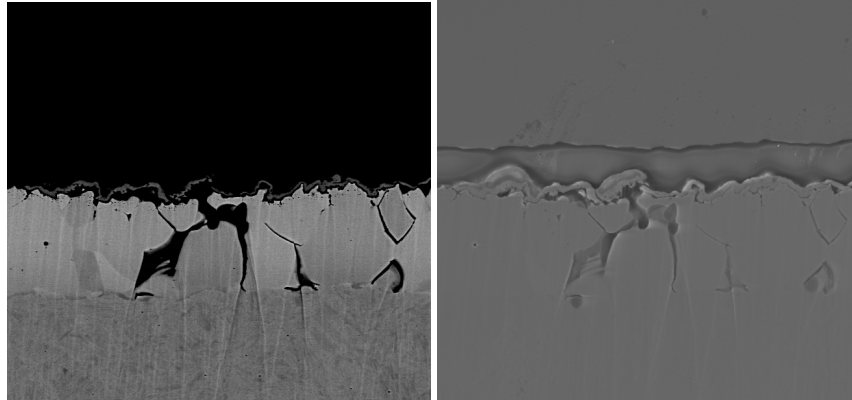


Figure 2.9: *Left*: BSE image of a zinc sample coated steel sheet. *Right*: SE image of the same area of the sample.

Topographic contrast

One of the most important uses of SEM is the visualization of topography. Both BSE and SE exhibit topographic contrast. This includes all the effects of the shape of the object. The numbers of BSE and SE electrons depend on the angle of the primary electron beam and the specimen.

The following effects are responsible for the formation of topographic contrast.

1. The number of BSEs increases by tilting the sample stage towards the detector. The same effect appears if the surface is locally tilted with respect to the detector.
2. The number of SEs varies with the specimen tilt angle with respect to the incident beam. The directionality of the detector does not matter because the electrons are collected by the biased Faraday cage or magnetic field in the through-lens detector.

The difference is that one side of a peak is bright in the BSE image, while the opposite side is dark, but both sides are bright on an SE image while the top is dark.

Edge Effect in SE

Observing brightness in SE images shows the range of SE escape. As shown in Figure 2.10, edges are brighter than interior regions. This happens because the number of SEs that escape at sample edges is much higher than elsewhere in the sample.

2.2 Optimization

Optimization is the process of minimizing or maximizing a function by selecting the best value for its variables within the domain. Without loss of generality, we can assume the

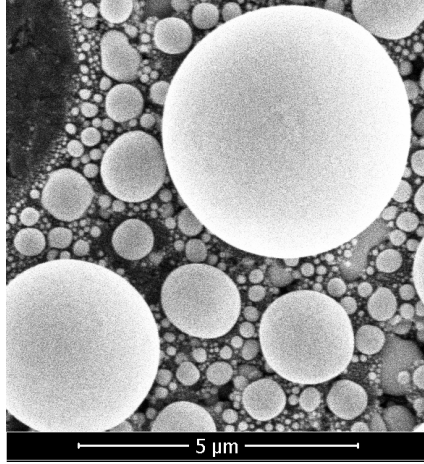


Figure 2.10: Edge effect on a tin sphere specimen.

function is being minimized. Concretely, we will work with functions defined on a subset of a real vector space, where the subset is defined by a set of equalities, and inequalities. To define the problem we need

1. a set of variables, which can be written as a vector $x \in R^n$,
2. a set of inequalities, $g_i(x) \leq 0$, for i in an index set,
3. a set of equalities, $h_i(x) = 0$, for i in a second index set, and
4. an objective function, $f(x)$, which is defined for at least all of the points $x \in R^n$ for which all of the inequalities and equalities are satisfied.

The problem is feasible if there are points satisfying all of the constraints and the set of such points is called the feasible set. The problem always has a solution in many practical cases, such as when the feasible set is bounded and the objective function is convex.

For the purpose of this thesis, we illustrate this with an example relevant to Chapter 4. For assigning a label to each pixel in an image like Figure 2.11 (left) it would be advantageous to know the mean greyscale value and number of pixels in each of the two regions. Computing the histogram (right) of the image on the left, we get an approximate distribution of pixel values, which looks like two overlapping normal distributions. Consequently, if we are able to fit the sum of two normal distributions each defined by

$$p_{\mu,\sigma}(k) = \frac{1}{\sqrt{2\pi\sigma^2}} e^{-\frac{(k-\mu)^2}{2\sigma^2}} \quad (2.3)$$

to the histogram, we would have an estimate for the mean value and population size which we could use for segmenting the image. Here μ is the mean value, σ is the standard deviation and k is the index.

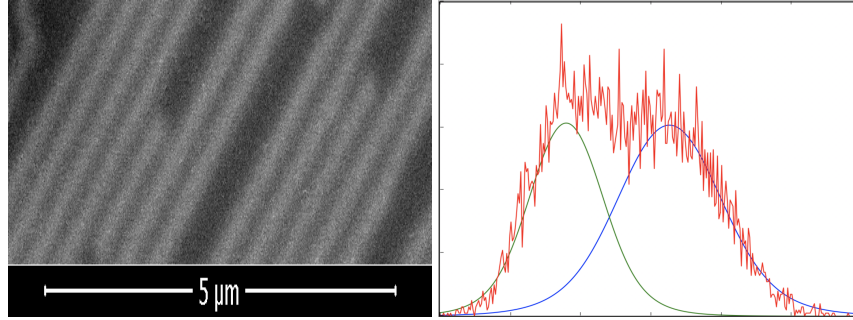


Figure 2.11: *Left*: a grayscale image part of an electronic circuit. *Right*: Red line is the image histogram with two greyscale values. Green and the blue line are two normal distribution that are minimized with the histogram by the optimization problem

If $q(k)$ represents the frequency of pixels in each interval of the range of greyscale values,

$$\min \sum_k \left(p_{1,\mu_1,\sigma_1}(k) + p_{2,\mu_2,\sigma_2}(k) - q(k) \right)^2, \quad 0 < \mu_1 \leq 300, 0 < \mu_2 \leq 300, \quad (2.4)$$

is the optimization problem for fitting the sum of two normal distributions to $q(k)$. This optimization problem is non-linear because it contains an exponential of a variable. It is constrained because we limit μ to lie between 0 and 300.

The result has been shown in Figure 2.11 the red line shows the frequency of pixels in each interval and the blue and green lines are the two normal distributions that the optimization problem produced.

2.2.1 Optimization Tools

There are several tools to implement optimization problems. We will use two open-source libraries, PuLP and Pyomo in Python. PuLP can call linear solvers such as CBC, GLPK, CPLEX and Gurobi. Although PuLP is just able to solve linear problems, Pyomo solves much more complicated models. It is able to solve following problem types:

1. Linear programming
2. Quadratic programming
3. Nonlinear programming
4. Mixed-integer linear programming
5. Mixed-integer quadratic programming
6. Mixed-integer nonlinear programming

7. Stochastic programming
8. Generalized disjunctive programming
9. Differential algebraic equations
10. Bilevel programming
11. Mathematical programs with equilibrium constraints

Pyomo supports many solvers such as AMPL, PICO, CBC, CPLEX, IPOPT, Gurobi and GLPK.

Many solvers are also available on NEOS, Czyzyk et al. (1999) a free website giving access to more than 60 solvers. It is Hosted by the Wisconsin Institute for Discovery at the University of Wisconsin in Madison. We can write programs in a modelling language like AMPL and upload the program file and its data on the website. The optimization problem will be solved on a server and it will send back the result by the webpage or an email.

Chapter 3

3D Reconstruction

Abstract

We present an optimization method for three-dimensional (3D) reconstruction from a small number of scanning electron microscope (SEM) images based on angle-of-incidence effects. At each of eight angles we acquire a Backscatter Electron (BSE) and Secondary Electron (SE) image using an Everhart-Thornley detector. Such images could be acquired in parallel, but our tests use eight stage rotations. Previous methods have obtained height information by integrating the difference of BSE images acquired at opposite angles. We use an optimization problem to find a single heightmap which best matches the slope information for four images differences, corresponding to four different directions. We show that this eliminates line artifacts caused by noise. Since BSEs are less sensitive than SEs to changes in slope near vertical (parallel to the electron beam), we propose a correction using the SE images to predict the slope, and use it to correct the magnitude of the slope in the heightmap obtained from the BSE images. We use an empirical model to convert SE image intensity to slope. We have validated the full method on tin spheres and the BSE-optimization problem on fabricated silicon test objects, using both AFM measurements and specifications.

3.1 Introduction

The 3D reconstruction of microstructure surfaces in Scanning Electron Microscope (SEM) images allows researchers to extract quantitative information regarding material morphology. This information is useful in the characterization and classification of materials and can aid in the prediction of the materials capabilities (Yan et al., 2017). Accurate quantitative information can also be used for quality control in microfabrication (Shishido et al., 2011).

There are two approaches to this problem, with some authors combining the two. One approach applies algorithms developed for optical images to SEM images. The second approach uses models for backscatter electron in SEM image contrast (BSE) from opposing directions.

Algorithms from optical imaging work best with many images, and are based on perspective, parallax and Lambertian shading, (Tafti et al., 2015). Previous work applying

optical imaging methods use photogrammetry in which hundreds of 2D images taken from different angles. In SEM imaging, this involves tilting and rotating the stage many times. This is time consuming, and is constrained by the proximity of the detectors to the stage, which is generally not a problem with optical imaging. Tafti et al. (2015) surveyed the expanding body of work in this area. They classified methods as single-view, multi-view or hybrid techniques. Some are quite sophisticated combinations of multiple techniques, for example the “sparse feature-based stereo rectification, nonlocal-based optical flow estimation for dense matching and finally depth estimation” implemented by Baghaie et al. (2017). Other methods go beyond qualitative surface shape reconstruction, to give estimates of surface area and volume, for example, Mulukutla et al. (2017) even have a method robust with respect to partial-object imaging.

Algorithms leveraging the intrinsic contrast of SEM images are based on the observation that SE and BSE signals depend continuously on the angle of the surface relative to the incident electron beam. For SE signals, Müller (1937) observed that the signal is approximately proportional to the secant of the slope relative to the perpendicular plane. Lebedzik (1975) calibrated the SE and BSE components and calculated the gradient of the surface from four BSE detectors. After further work to eliminate the SE component from the images, Lebedzik (1979) then proposed that, given BSE images collected by detectors at opposing angles, which he called I_0 and I_{180} , the slope could be calculated as

$$\frac{\partial h}{\partial x} = D \tan \left(\arcsin \frac{I_0 - I_{180}}{I_0 + I_{180}} \right), \quad (3.1)$$

where $h(x, y)$ is the height of the sample, and (x, y) are the usual coordinates, with 0° along the positive x -axis. Integrating this equation yields $h(x, y)$ if the height along the edge of the sample is known. The reason that the image difference was normalized by dividing out $I_0 + I_{180}$ is that this eliminated residual SE signal resulting in bright edge effects.

This was extended to surfaces by scanning lines by Suganuma (1985) and Kholodilov et al. (1987). Both use variations on (3.1), with Suganuma finding a better fit to the slope by taking the squares of pixel intensities before subtracting, and Kholodilov et al, normalizing by the first image. It was also extended by Carlsen (1985) who observed that noise in the acquisition accumulated via the process of integration, but that integrating in different directions could compensate for this. His approach was to set up a large system of linear equations, representing multiple paths of integration, and solving it in the least-squares sense. This is essentially a special case of this paper’s model (QM-BSE), with four images, but solved as an over-determined system of linear equations using multi-grid methods. The computational resources available at the time did not make this method practical. Subsequent work reverted to the computationally simpler approach of integrating along parallel lines, or in some cases integrating along one direction and then the perpendicular direction (Drzazga et al., 2005), or in the case that both image differences are corrupted by shadows, constructing synthetic images equivalent to rotating the stage by 45° and integrating along diagonals. Chen et al. (2012) iteratively correct for shadows in the source BSE images, taken from opposite angles, caused by raised features. Miyamoto et al. (2014) add self-calibration and image segmentation, but there are still problems with densely packed features, for which it was necessary to add segmentation and comparison to the features as designed (meaning the technique can only be applied for quality control of manufactured objects) (Miyamoto et al., 2017).

The approximate linear relationship in (3.1) is an empirical observation, but it was validated using a Monte Carlo simulations of electron trajectory as a function of angle by

Desai & Reimer (1990), for incident angles less than 40° . Authors generally do not correct for the lack of linearity at higher incident angles.

Finally, it is possible to combine geometric methods and pixel-difference methods (also called shape from shading), and potentially benefit from the strengths of both algorithms. This was demonstrated by Beil & Carlsen (1991), and continues to be developed, for example Yan et al. (2017) demonstrated this approach on geologic samples with many corner features, and planar or nearly planar facets.

This paper presents two improvements to this method. Firstly, we consider multiple pairs of opposite angle images, giving different projections of the gradient of the surface, and formulate and solve optimization problems to combine these into a single surface. With only one pair of images, this method would reduce to integration of the slope, but with multiple pairs, it finds the surface which best matches the slope in all of the measured directions. Secondly, we address a known weakness with the linear model, namely that it is not accurate for near-vertical slopes. To do this, we augment the information from the paired BSE images with information from SE images. Unlike BSE images which have similar contrast to optical images with a single light source, SE images have an edge effect, in which brightness increases as the slope approaches the vertical (Goldstein et al., 2017). This is a fundamentally non-linear effect, and depends on the maximum slope, not on one component of the gradient. We have developed an empirical model to translate brightness into this slope. This approach would work with any number of paired images, and could be adapted to use directional SE images, but we will present an implementation with utilizing eight SEM images collected using an off-centre Everhart-Thornley detector (ETD) in backscatter electron (BSE) mode, and composite SE images formed by adding the images collected at the same eight angles. Scan time would be shorter on a machine with a segmented BSE detector or multiple ETDs capable of simultaneous acquisition. With enough detectors, all images could be acquired simultaneously.

We will present two optimization approaches, one using Linear Programming (with ℓ_1 norms) and Nonlinear Programming (with ℓ_2 norms). This paper proposes a model-based reconstruction method that is formulated as an optimization problem. This method utilizes eight images collected using an ETD detector in BSE mode. The first implementation of this work uses the ℓ_1 norm as it results in a linear program.

3.2 Theory

As explained in the introduction, there are several similar empirical models relating the difference of BSE signal from opposite detectors to slope. We use our own variation

$$\frac{\partial h}{\partial x} = D \left(I_0^2 - I_{180}^2 \right), \quad (3.2)$$

which uses the difference of squared pixel values, without division to reduce the impact of SE edge effect, and without the trigonometric functions. This approximation is most similar to the approximation used by Suganuma (1985). We have tried other variations, but none performed better, and this formulation is simpler. In particular, arcsin is inherently sensitive to normalization because it is undefined outside the interval $[-1, 1]$. Normalizing by $I_0 + I_{180}$, in (3.1), prevents this problem, but biases the results away from extreme angles because $\frac{I_0 - I_{180}}{I_0 + I_{180}}$ can only be ± 1 when one of I_0 or I_{180} is zero, since images are non-negative,

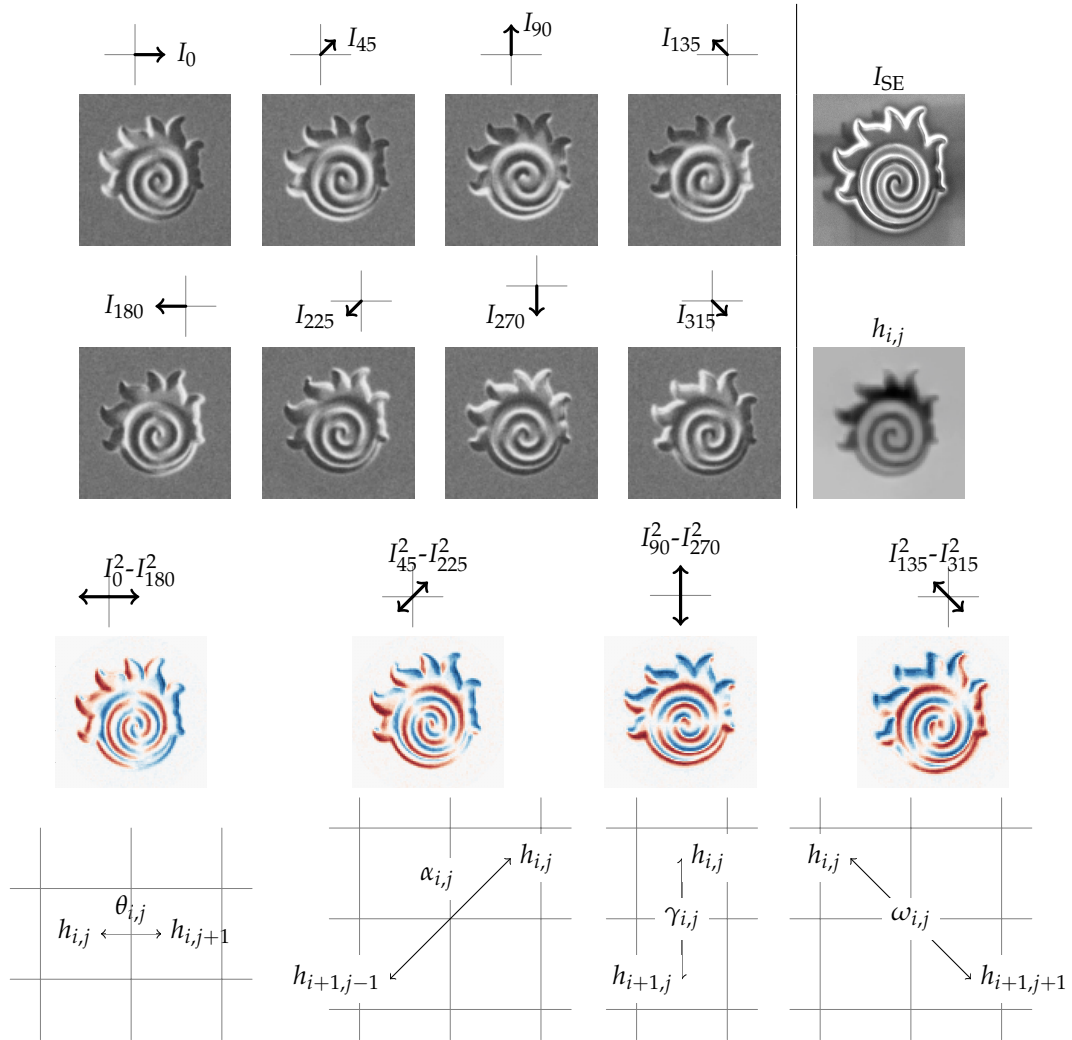


Figure 3.1: This method uses eight BSE images taken from different angles by rotating the sample stage (*top left*); and the sum of SE images taken at the same angles (*top-right upper*). In the first problem, the squares of the opposite BSE images are subtracted (*middle*), and these values are compared in the optimization problem to differences in the heightmap ($h_{i,j}$, *top-right lower*) of the appropriate neighbouring pixels. The calculation of each absolute value requires a parameter ($\theta, \alpha, \gamma, \omega$) (*bottom*).

and, in practice, the images are never zero, except for voids. This is the mathematical “explanation” for the lack of linearity at higher incident angles. Trying to correct this would

magnify the error. Fortunately, this is exactly where the SE signal provides high-quality information, as we will explain below.

Previous approaches have ignored noise and integrated (3.2) along lines, using discretization to obtain

$$h_{i,j+1} - h_{i,j} = D' \left(I_{0i,j}^2 - I_{180i,j}^2 \right) \quad (3.3)$$

Solving the system of equations given by (i_0, j) for a fixed row, i_0 , in the image is equivalent to integrating the discrete approximation. Given more than two images, e.g., adding I_{90} and I_{270} , introduces additional equations, which cannot all be solved simultaneously. So instead, we turn each equation into a cost component, and seek to minimize the total cost. There are two common approaches,

$$\left| (h_{i,j+1} - h_{i,j}) - D' \left(I_{0i,j}^2 - I_{180i,j}^2 \right) \right|, \quad (3.4)$$

or

$$\left((h_{i,j+1} - h_{i,j}) - D' \left(I_{0i,j}^2 - I_{180i,j}^2 \right) \right)^2, \quad (3.5)$$

corresponding to distance in the ℓ_1 norm, (3.4), also called Manhattan distance, or the ℓ_2 normal, (3.5), also called the energy. The first approach can be encoded as a linear program, the second as least-squares optimization problem.

In this paper, we will use eight images, see Figure 3.1. This requires the use of diagonal differences, as can be seen in Figure3.1, which are longer by a factor of $\sqrt{2}$. We are now ready to formulate models which take the BSE images as input and output heightmaps which we refer to as h^b , since they do not incorporate all the image information.

3.2.1 Linear Model (LM-BSE)

$$\begin{aligned} \min \quad & \sum_{i,j} \theta_{i,j} + \sum_{i,j} \alpha_{i,j} + \sum_{i,j} \gamma_{i,j} + \sum_{i,j} \omega_{i,j} + \lambda \sum_{i,j} \sigma_{i,j} \\ \text{s.t.} \quad & (I_0^2 - I_{180}^2)_{i,j} - (h_{i,j+1}^b - h_{i,j}^b) \leq \theta_{i,j} \\ & (h_{i,j+1}^b - h_{i,j}^b) - (I_0^2 - I_{180}^2)_{i,j} \leq \theta_{i,j} \\ & (I_{45}^2 - I_{225}^2)_{i,j} - \frac{1}{\sqrt{2}}(h_{i+1,j-1}^b - h_{i,j}^b) \leq \alpha_{i,j} \\ & \frac{1}{\sqrt{2}}(h_{i+1,j-1}^b - h_{i,j}^b) - (I_{45}^2 - I_{225}^2)_{i,j} \leq \alpha_{i,j} \\ & (I_{90}^2 - I_{270}^2)_{i,j} - (h_{i+1,j}^b - h_{i,j}^b) \leq \gamma_{i,j} \\ & (h_{i+1,j}^b - h_{i,j}^b) - (I_{90}^2 - I_{270}^2)_{i,j} \leq \gamma_{i,j} \\ & (I_{135}^2 - I_{315}^2)_{i,j} - \frac{1}{\sqrt{2}}(h_{i+1,j+1}^b - h_{i,j}^b) \leq \omega_{i,j} \\ & \frac{1}{\sqrt{2}}(h_{i+1,j+1}^b - h_{i,j}^b) - (I_{135}^2 - I_{315}^2)_{i,j} \leq \omega_{i,j} \\ & (-h_{i,j}^b + h_{i+1,j}^b + h_{i,j+1}^b - h_{i+1,j+1}^b) \leq \sigma_{i,j} \\ & -(-h_{i,j}^b + h_{i+1,j}^b + h_{i,j+1}^b - h_{i+1,j+1}^b) \leq \sigma_{i,j} \end{aligned}$$

Where the variable $h_{i,j}^b$ is indexed by the pixel location (i, j) corresponding to the row and column in the image, the variables $\theta_{i,j}$, $\alpha_{i,j}$, $\gamma_{i,j}$ and $\omega_{i,j}$ are used to encode the absolute values, and $\sigma_{i,j}$ is used for regularization. The image values, I , defined by Figure 3.1, are constants in the optimization problem. Note that we have dropped the scale factor D , because in the next step we will only use the direction of ∇h^b , and the scaling will be irrelevant. This model has the advantage that many open-source and commercial linear solvers are available, and able to efficiently solve very large problems (with billions of variables).

The quadratic model is simpler to write out, because it does not require helper variables to encode the absolute value.

3.2.2 Quadratic Model (QM-BSE)

$$\begin{aligned} \min \sum_{i,j} & \left((I_0^2 - I_{180}^2)_{i,j} - (h_{i,j+1}^b - h_{i,j}^b) \right)^2 \\ & + \sum_{i,j} \left((I_{45}^2 - I_{225}^2)_{i,j} - \frac{1}{\sqrt{2}}(h_{i+1,j-1}^b - h_{i,j}^b) \right)^2 \\ & + \sum_{i,j} \left((I_{90}^2 - I_{270}^2)_{i,j} - (h_{i+1,j}^b - h_{i,j}^b) \right)^2 \\ & + \sum_{i,j} \left((I_{135}^2 - I_{315}^2)_{i,j} - \frac{1}{\sqrt{2}}(h_{i+1,j+1}^b - h_{i,j}^b) \right)^2 \\ & + \lambda \sum_{i,j} \left(-h_{i,j}^b + h_{i+1,j}^b + h_{i,j+1}^b - h_{i+1,j+1}^b \right)^2 \end{aligned}$$

Regularization in optimization is an approach to balancing fit to noisy data with a priori assumptions about the solution, most often assumptions about smoothness or continuity. The equation

$$-h_{i,j}^b + h_{i+1,j}^b + h_{i,j+1}^b - h_{i+1,j+1}^b = 0 \quad (3.6)$$

is satisfied for the four neighbouring discretized heights if those four points are coplanar. Adding the ℓ_1 or ℓ_2 norm of the deviation works similarly to the other cost terms, and we add a scale λ , called a penalty or regularization parameter to balance the data fidelity versus smoothness. The regularization parameter can be chosen using a method based on the ‘‘L-curve’’ (Hansen & O’Leary, 1993) but is often chosen empirically. We use $\lambda = 1$, based on empirical observation, but this problem is not very sensitive to λ and values from 1/10 to 10 work well.

3.2.3 Adding SE Mode Information

The problem with all of the BSE/height models is that they are only valid for some slopes. Authors differ on whether they are reliable above 60° or 80° , but they are not accurate for steep slopes. On the other hand, SE-mode images, see Figure 3.2, are very sensitive to high slopes and insensitive to low slopes. Our next pair of models attempt to correct h^b in regions of high slope.

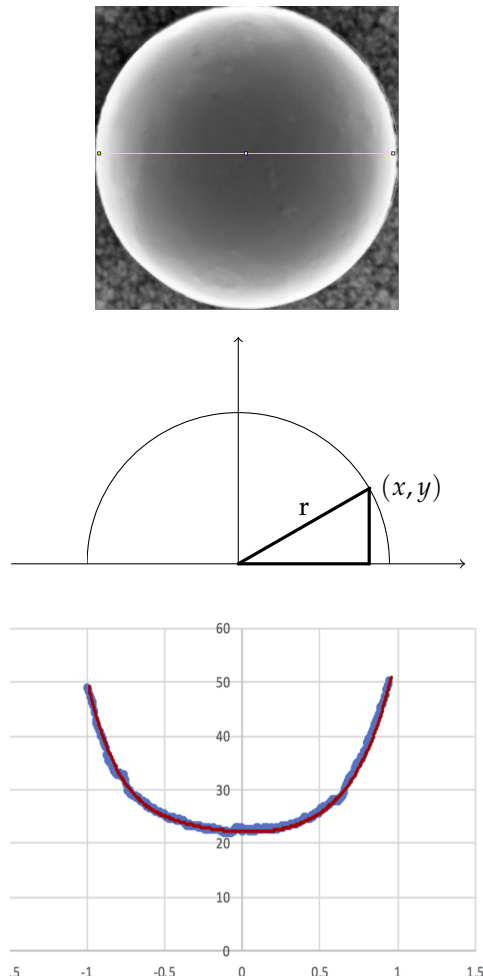


Figure 3.2: *Top*: Sum of eight SE images; *middle*: definition of variables; *bottom*: profile plot of yellow line on the SE image, with best-fit even quartic $y = 25.753x^4 + 3.89x^2 + 22.487$.

The problem with the SE-mode images is that they are primarily dependent on absolute slope and not on the direction of the slope, i.e., the full gradient. The dependence on the direction includes complicated shadowing effects determined by the geometry of other objects and the detectors. We have found that adding the SE-mode images from all directions produces an image with essentially only slope dependence. We will therefore present models which assume that a “directionless” SE-mode image is available. Theoretically, we expect SE images to be directionless, because SEs are low-energy electrons subject to the Faraday cage potential on the ETH and are therefore collected independently of the sample orientation.

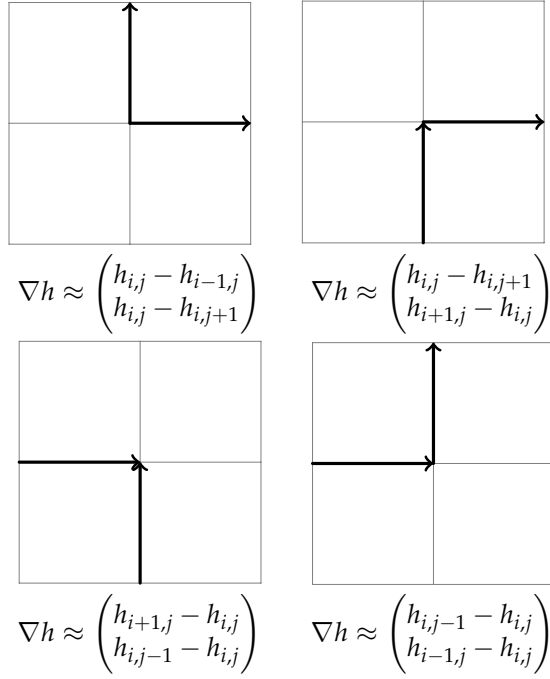


Figure 3.3: Four discrete gradient approximations.

To determine the dependence of the SE-mode intensity on the slope, we plotted a cross-section of a sphere, used the equation for the sphere to convert position into slope, and then fit an even quartic polynomial,

$$y = ax^4 + bx^2 + c, \quad (3.7)$$

to the slope versus intensity scatter plot, see Figure 3.2. Since the pixel intensities are constants in the optimization problem, the use of quadratic polynomials (or more complicated functions) does not change the class of the optimization problem. Using (3.7), we calculate the equivalent radius for each pixel as

$$x_{i,j}^2 = \frac{2(c - I_{SE,i,j})}{-b - \sqrt{b^2 - 4a(c - I_{SE,i,j})}}, \quad (3.8)$$

where we have substituted the SE-mode pixel values for y and applied the quadratic formula. We omit this small number of pixels from SE-mode terms in the subsequent optimization model. The slope at each pixel is then

$$s_{i,j} = \sqrt{\frac{x_{i,j}^2}{1 - x_{i,j}^2}}. \quad (3.9)$$

Note that, due to noise, the denominator may be negative, making the slope undefined.

Given the slope $s_{i,j}$, we would like $|\nabla h| = s$ at all remaining pixels, but we observed numerical problems in regions of high slopes, for example in Figure 3.4, we see that the usual discretized gradient has obvious errors. To get around this, we consider the multiple ways of approximating the gradient, shown in Figure 3.3, and for each pixel we take the minimum magnitude result, which is also shown in Figure 3.4.

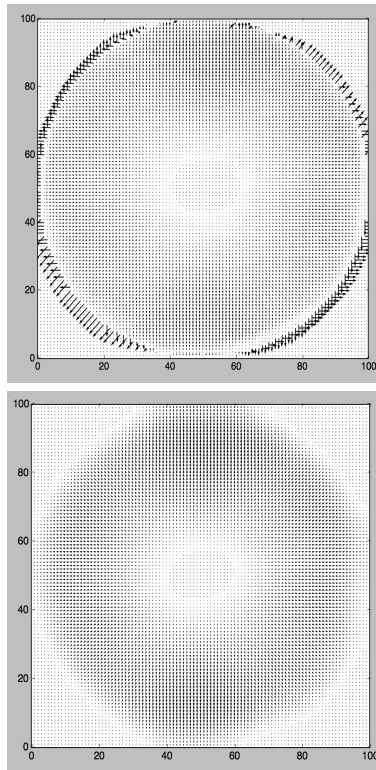


Figure 3.4: *Top*: Numerical errors caused by a fixed gradient discretization, $G_{0,i,j}$. *Bottom*: $G_{k_{i,j},i,j}$ the minimizing case.

Define the four different gradient approximations as

$$G_{i,j} = G_{k_{i,j},i,j}, \quad \text{for } k = 0, 1, 2, 3. \quad (3.10)$$

Let k be indices indicating the minimal-length case:

$$k_{ij} = \operatorname{argmin}_{k \in \{0,1,2,3\}} |G_{k,i,j}|. \quad (3.11)$$

The two components of the gradient are then defined to be

$$G_{\downarrow,i,j} = \begin{cases} h_{i,j}^b - h_{i-1,j}^b & k_{i,j} = 0 \\ h_{i,j}^b - h_{i,j+1}^b & k_{i,j} = 1 \\ h_{i+1,j}^b - h_{i,j}^b & k_{i,j} = 2 \\ h_{i,j-1}^b - h_{i,j}^b & k_{i,j} = 3 \end{cases} \quad (3.12)$$

and

$$G_{\leftrightarrow,i,j} = \begin{cases} h_{i,j}^b - h_{i,j+1}^b & k_{i,j} = 0 \\ h_{i+1,j}^b - h_{i,j}^b & k_{i,j} = 1 \\ h_{i,j-1}^b - h_{i,j}^b & k_{i,j} = 2 \\ h_{i,j}^b - h_{i-1,j}^b & k_{i,j} = 3 \end{cases} \quad (3.13)$$

To further reduce the impact of noise, we smooth the resulting gradients, letting $G'_{\downarrow,i,j}$ and $G'_{\leftrightarrow,i,j}$ be $G_{\downarrow,i,j}$ and $G_{\leftrightarrow,i,j}$ respectively with a radius-four Gaussian filter applied, and \tilde{G} be G' normalized to be of unit length. To avoid division by zero, we normalize with a safe scale factor and s calculated from the SE image above:

$$\tilde{G} = \frac{s}{|G'| + \epsilon} \cdot G' \quad (3.14)$$

This defines the expected gradient, which we match with similarly calculated approximate gradients

$$H_{\downarrow,i,j} = \begin{cases} h_{i,j} - h_{i-1,j} & k_{i,j} = 0 \\ h_{i,j} - h_{i,j+1} & k_{i,j} = 1 \\ h_{i+1,j} - h_{i,j} & k_{i,j} = 2 \\ h_{i,j-1} - h_{i,j} & k_{i,j} = 3 \end{cases} \quad (3.15)$$

and

$$H_{\leftrightarrow,i,j} = \begin{cases} h_{i,j} - h_{i,j+1} & k_{i,j} = 0 \\ h_{i+1,j} - h_{i,j} & k_{i,j} = 1 \\ h_{i,j-1} - h_{i,j} & k_{i,j} = 2 \\ h_{i,j} - h_{i-1,j} & k_{i,j} = 3 \end{cases} \quad (3.16)$$

using the same minimizing indices $k_{i,j}$.

Finally, to combine the BSE and SE information we use a weighting factor,

$$w = \frac{e^{2(I_{SE_{i,j}} - 0.5)}}{1 + e^{2(I_{SE_{i,j}} - 0.5)}} \quad (3.17)$$

which is 1 at pixels with near-infinite slope, and 0 at pixels with 0 slope, and has intermediate values for intermediate slopes, reflecting the relative information in the two signals.

Linear BSE+SE Optimization Problem

$$\begin{aligned}
\min \quad & \sum_{i,j} (1 - w_{i,j}) \theta_{i,j} + \sum_{i,j} (1 - w_{i,j}) \alpha_{i,j} + \sum_{i,j} w_{i,j} \beta_{i,j} \\
& + \sum_{i,j} (1 - w_{i,j}) \omega_{i,j} + \sum_{i,j} (1 - w_{i,j}) \gamma_{i,j} + \sum_{i,j} \sigma_{i,j} \\
\text{s.t.} \quad & (I_0^2 - I_{180}^2)_{i,j} - (h_{i,j} - h_{i,j+1}) \leq \theta_{i,j} \\
& (h_{i,j} - h_{i,j+1}) - (I_0^2 - I_{180}^2)_{i,j} \leq \theta_{i,j} \\
& (I_{45}^2 - I_{225}^2)_{i,j} - \frac{1}{\sqrt{2}}(h_{i,j} - h_{i+1,j-1}) \leq \alpha_{i,j} \\
& \frac{1}{\sqrt{2}}(h_{i,j} - h_{i+1,j-1}) - (I_{45}^2 - I_{225}^2)_{i,j} \leq \alpha_{i,j} \\
& (I_{90}^2 - I_{270}^2)_{i,j} - (h_{i,j} - h_{i+1,j}) \leq \gamma_{i,j} \\
& (h_{i,j} - h_{i+1,j}) - (I_{90}^2 - I_{270}^2)_{i,j} \leq \gamma_{i,j} \\
& (I_{135}^2 - I_{315}^2)_{i,j} - \frac{1}{\sqrt{2}}(h_{i,j} - h_{i+1,j+1}) \leq \omega_{i,j} \\
& \frac{1}{\sqrt{2}}(h_{i,j} - h_{i+1,j+1}) - (I_{135}^2 - I_{315}^2)_{i,j} \leq \omega_{i,j} \\
& (-h_{i,j} + h_{i+1,j} + h_{i,j+1} - h_{i+1,j+1}) \leq \sigma_{i,j} \\
& -(-h_{i,j} + h_{i+1,j} + h_{i,j+1} - h_{i+1,j+1}) \leq \sigma_{i,j} \\
& H_{\downarrow,i,j} - \tilde{G}_{\downarrow,i,j} \leq \beta_{i,j} \\
& -H_{\downarrow,i,j} + \tilde{G}_{\downarrow,i,j} \leq \beta_{i,j} \\
& H_{\leftrightarrow,i,j} - \tilde{G}_{\leftrightarrow,i,j} \leq \beta_{i,j} \\
& -H_{\leftrightarrow,i,j} + \tilde{G}_{\leftrightarrow,i,j} \leq \beta_{i,j}
\end{aligned}$$

Quadratic BSE+SE Optimization Problem

$$\begin{aligned}
\min \sum_{i,j} & \left((I_0^2 - I_{180}^2)_{i,j} - (h_{i,j+1}^b - h_{i,j}^b) \right)^2 \\
& + \sum_{i,j} \left((I_{45}^2 - I_{225}^2)_{i,j} - \frac{1}{\sqrt{2}}(h_{i+1,j-1}^b - h_{i,j}^b) \right)^2 \\
& + \sum_{i,j} \left((I_{90}^2 - I_{270}^2)_{i,j} - (h_{i+1,j}^b - h_{i,j}^b) \right)^2 \\
& + \sum_{i,j} \left((I_{135}^2 - I_{315}^2)_{i,j} - \frac{1}{\sqrt{2}}(h_{i+1,j+1}^b - h_{i,j}^b) \right)^2 \\
& + \sum_{i,j} \left(H_{\uparrow,i,j} - \tilde{G}_{\uparrow,i,j} \right)^2 \\
& + \sum_{i,j} \left(H_{\leftrightarrow,i,j} - \tilde{G}_{\leftrightarrow,i,j} \right)^2 \\
& + \lambda \sum_{i,j} \left(-h_{i,j}^b + h_{i+1,j}^b + h_{i,j+1}^b - h_{i+1,j+1}^b \right)^2
\end{aligned}$$

3.3 Methods

Our algorithm was implemented in Python 3.5.2 from the Anaconda 4.1.1 distribution running on macOS 10.13.6. Linear optimization was performed using PuLP version 1.6.8. Nonlinear optimization was performed using Pyomo version 5.5.0 calling Ipopt version 3.12.9.

Imaging

Images were acquired using a Thermo Fisher FEI Magellan 400. This device is equipped with a computer controlled stage, enabling movements in x, y and z directions well as tilt (-10° to 60°) and rotation (0 to 360°). The SEM images were centred manually after each of eight rotations, using an accelerating voltage of 5 kV and current of 50pA. Signals were acquired from the Everhart-Thornly detector, in both high- and low-bias modes. In both BSE and SE modes, the brightness and contrast levels were set to ensure that the full dynamic range of the detectors was employed. For all measurements of one type, the detectors were set at the same brightness and contrast.

3.4 Results

The first innovation in our approach is the combination of integration along multiple directions in a single optimization problem. Figure 3.5 shows the result of integrating in a single direction next to the result of solving the linear BSE-only optimization problem. The obvious streaking is the result of noise in each line integrating across the line without reference to neighbouring lines.

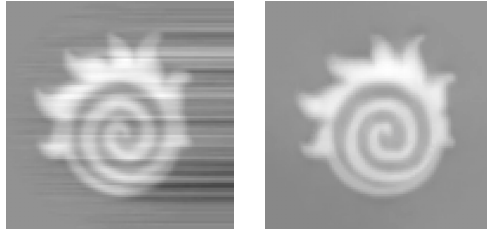


Figure 3.5: *Left:* Result of integrating $I_0^2 - I_{180}^2$ along the x-axis. *Right:* Result of solving LM-BSE.

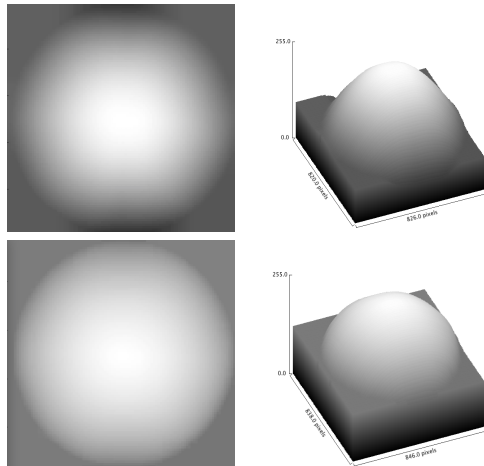


Figure 3.6: SE information produces rotationally symmetric and rounder ball. *Top:* two views of the heightmap h^b produced by the first linear model. *Bottom:* two views of the heightmap h produced by the second linear model which uses the direction of ∇h^b and the SE images.

The second innovation involves the combination of SE-mode information with the difference of BSE-mode images. Figure 3.6 shows the results for a single tin ball in which the top BSE-only results are clearly not rotationally symmetric (left) and not very round (right), whereas the bottom BSE+SE results are visibly rotationally symmetric, and much rounder.

Finally, we produced a number of test objects, fabricated using focused ion beam

(FIB) patterning, collected both SEM images and Atomic Force Microscopy (AFM) data for comparison. Figure 3.7 shows three of our test objects fabricated in a silicon substrate. For each we show one BSE and one SE source image, the AFM heightmap represented as an image and a 3D rendering, as well as the BSE-only heightmap represented as an image and a 3D rendering. We did not apply the BSE+SE problem to these examples, because we have not calibrated the SE intensity for silicon. Both the AFM probe and our method have limitations which make it hard to quantify the accuracy of our algorithm, but we are satisfied with them qualitatively. For example, the AFM probe (with thickness 10nm, and probe angle 20°) was not able to track the narrow trenches with sharp angles in the Fireball, whereas it reported the depths of the trenches in the third test object to be close to equal, whereas our method computed shallower depths for the narrower trenches.

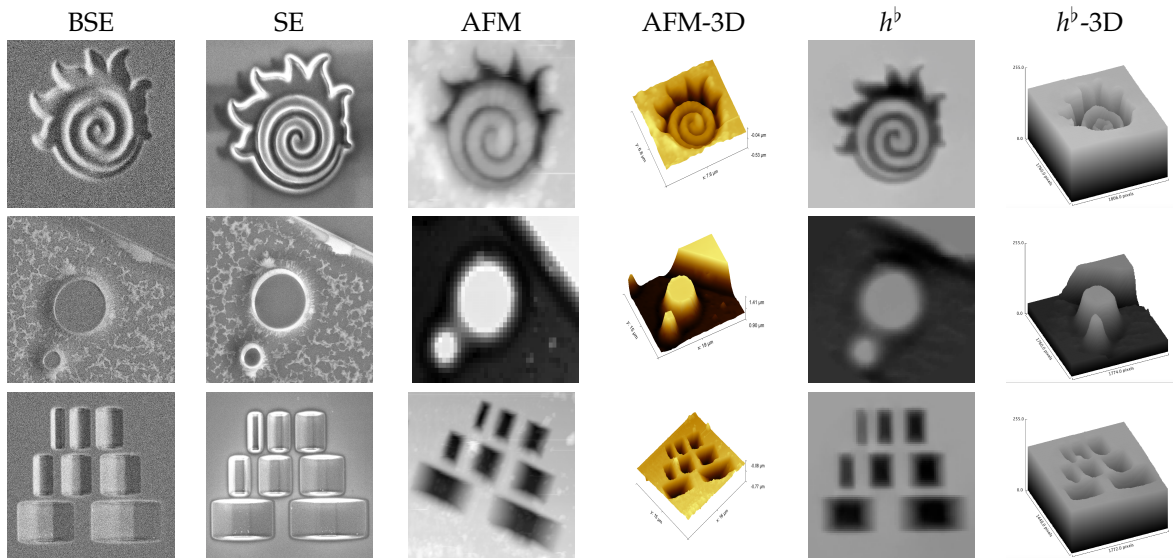


Figure 3.7: Validation of the method on silicon test objects: McMaster Fireball, towers and trenches. The columns show sample BSE and SE images, the AFM heightmap, a 3D rendering of the AFM heightmap, the optimized heightmap, h^b and a 3D rendering thereof. Of note are the the limitations of the AFM to probe the narrow trenches in the top sample, the accuracy of h^b in representing the trenches surrounding the test towers and the edge of the cut region, in agreement with the AFM probe, in the middle sample.

3.5 Discussion

We have demonstrated the feasibility of incorporating both SE and BSE images to improve the performance of surface reconstruction from intrinsic shading, by relying on BSE images for regions of shallow slope and SE images to correct steep slopes. This integrated approach is also inherently insensitive to noise. While we have demonstrated the approach with eight images, it could be generalized to any number of image pairs.

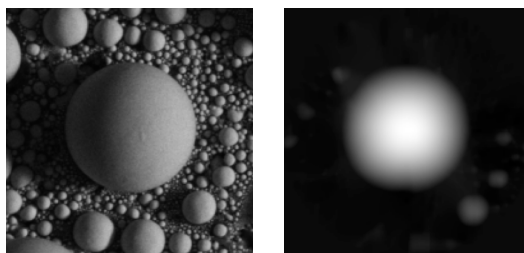


Figure 3.8: *Left*: One of eight ETD-BSE-mode images of sputtered tin balls. *Right*: Optimized heightmap h^b , in which most of the smaller balls are missing.

3.5.1 Future Work

In Figure 3.8, we show a larger view of the tin-ball sample, which is obviously missing some smaller balls which are shadowed by the central ball from some angles. We speculate that this is caused by the known difficulty with shadows of larger objects, and that this is at least part of the reason that the narrow trenches appear shallower on our heightmap than the AFM heightmap. Recall that other objects effect imaging in two ways: by blocking the scanning electron beam, and by blocking (some of) the returning electrons which would have otherwise reached the detector. As mentioned in the introduction, the compensation for shadows is an open research problem, and is acknowledged to be computationally more difficult than height-map reconstruction without shadows, but there are approaches we could try to adopt. Most other approaches use an iterative approach (Miyamoto et al., 2017), or rely on information from photogrammetry (Yan et al., 2017). Since our optimization approach is built by adding cost functions, we would like to try incorporating shadow detection as an additional cost term or terms. Extending this approach, we could also reconstruct some surface features not visible from above, but this would be limited without tilting the stage for additional images. Depending on the application the extra time required to tilt the stage and collect an image may be justified.

We did not attempt to use SE intensity information with silicon sample objects because our method of calibration depended on identifying a sphere, and tin spheres were readily available. There are three other approaches we would like to consider for calibrating the correspondence between SE intensity and slope. The first approach would be to consider a $|\nabla h^b|$ versus SE scatterplot of all pixel values. We have observed that this plot has a high-density curve which we believe to be parametrized by the slope. If we can determine the parameterization, then we can use the inverse to map SE intensity to slope, but we could also correct the non-linearity in the BSE/gradient-component relationship. The second approach would be to add a parameterized model for the relationship to the optimization problem, and simultaneously fit the model and the heightmap. The third approach (or more likely an adjunct to the first two) would be to use Monte Carlo simulations of SE effects, see Li & Ding (2005), to build a model or surrogate model of the relationship. This problem would be non-linear, but separable, and might be amenable to a Gauss-Seidel iteration, or an iteration similar to the one employed by Anand et al. (2004).

As with most papers in this area, all of our tests were performed with mono-element structures (Sn or Si). This allows us to ignore the dependence of scattering probability on composition. In theory the BSE model is not sensitive to chemical composition, because it uses a ratio, in which a multiplier of pixel intensity would cancel out, but we have not tested this. Furthermore, complexity will increase if there is varying height as well as lateral chemical heterogeneity in the structure. On the other hand, the SE model would be sensitive to chemical composition, including contamination such as carbon deposits and residue from FIB cutting, and this would need to be calibrated. In particular, the empirical model (3.7) would need to be calibrated for each material. We hope to be able to add fitting of multiple (3.7) models using localized pixel intensity histograms as a next step in the development of this method.

We developed linear and quadratic models because linear models can be solved more quickly, all else being equal, while nonlinear models are more flexible. Practically, these models may not be equally available to other researchers. Commercial software may be too expensive, or may be difficult to interface with, but open source software also has issues. Our PuLP implementation of the linear model takes 336s to solve a 100×100 image segment. Our Pyomo implementation of the quadratic model takes 9s, but it is difficult to install the underlying Ipopt library. While we are happy to share both implementations, we hope to develop an implementation which would be performant and easy to install.

Finally, our validation work was performed on an SEM capable of collecting one ETD image at a time. Newer instrumentation can collect multiple images in parallel, and there is no technological reason we could not collect all of the images we require during a single scan of the electron beam. Different detectors will require different calibrations, but would be worth the effort if they substantially accelerate image acquisition.

3.6 Acknowledgments

We are grateful to many research scientists at the Canadian Centre for Electron Microscopy for providing their help and expertise. We also would like to thank Christopher Schankula for his help on this project.

Chapter 4

Segmentation of SEM Images for Reverse Engineering

Abstract

In this paper, we present an optimization method for first completing sparse Scanning Electron Microscope (SEM) images and second segmenting completed images. Reducing scan time is always a challenge in SEM. Skipping lines while scanning is one way to speed up this process. In this work we propose an optimization method to complete a partial image. The resulting completed images are used as a starting point for a second optimization method which uses simultaneously acquired partial InLens and BSE images as input and produces a segmentation into three regions as the output. Both steps use regularization with L2 norms. The different noise characteristics of the two images are compensated for by convolving with a kernel design to match the point-spread function of observed noise, thought to be shot noise. The segmentation problem also uses a non-convex polynomial regularizer. We have validated this method on silicon-based semiconductor circuit samples with three separate segments, skipping three of every four lines, producing an acceleration of 4X. We found our results match manually segmented images. The amount of acceleration possible will depend on the material being scanned and experimental parameters.

4.1 Introduction

Since the process of imaging is time consuming, collecting partial noisy images and completing them using optimization can make imaging faster. For example, by collecting every fourth scan line in an image we could make the process of imaging four times faster. If the goal is to segment images, a more complicated optimization problem can be formulated. Completing images from partial data is a good way of making an initial guess for segmentation. Modern electron microscopes have multiple detectors capable of simultaneous image capture. Image fusion allows us to use this information without making the imaging process longer.

Image fusion has been used with SEM previously, but for different purposes. Milillo et al. (2015) combine optical microscopy and SEM images to get a better overall image. They

combine a high-resolution, low-information image with a low-resolution, high-chemical-information image to get a hybrid high-resolution, high-information image. Tarolli et al. (2014) uses the higher intensity and, hence, spatial resolution of the electron images to improve the quality of the secondary ion mass spectrometry (SIMS) images without sacrificing chemical specificity.

Segmentation is the process of assigning labels to different pixels of an image such that pixels with the same label share the same characteristics. Segmentation of SEM images has often been used to separate different phases of an image. Salzer et al. (2012) designed a segmentation algorithm for highly porous materials. It detects and allocates structures based on their last occurrence in the z-direction and then it improves the result by local thresholding. This method is suitable for natural materials, in which particles extend through multiple frames. Vromen & McCane (2009) use contour fitting and contour filtering to segment red blood cells, again suitable for biological samples. Sim et al. (2008) use a combination of Canny edge detection, optimization and supervised segmentation starting with a partial labeling by the user. It would be too time-consuming for our application. Kreshuk et al. (2011) uses machine learning techniques, but generating training data would again be time-consuming. The most common approach is a combination of thresholding, filtering, region growing etc., like Yang & Buenfeld (2001).

Unfortunately, as we show in Figure 4.1 on the left, thresholding might assign the wrong labels to pixels due to noise, and also on the right, we show that thresholding after filtering (with Gaussian filter) can cause distinct wire components to be connected. Similarly, in Figure 4.2 you can see how Canny edge detection fails to detect edges in such noisy images.

4.2 Semiconductor Circuits

In the images for this study, we are analyzing semiconductor circuit metallization lines. We can assume the circuits we image have two distinguishable components, metal and silicon, with three visible structures: silicon without metal, metal wires under a layer of silicon, and metal vias (through-plane wires connecting different layers). Figure 4.3 shows a typical example of this structure, with five layers of metallization. To image such samples, the upper layers are cut away to a horizontal plane which intersects the vias, the sample is then polished. Because the vias connect wires in upper and lower metallization layers, they appear “within” wires in the resulting image. Because the metal of the vias is exposed by this process, the vias are the brightest features of the image because they have the highest amount of high atomic number material at those pixels. Each sample has a characteristic wire size, with little variation, and regular patterns which are repeated throughout each layer.

4.2.1 Data

For imaging we use two detectors: InLens and BSE. These images can be collected simultaneously so that they are aligned. In Figure 4.4 you can see an images from the same part of a chip using the two different detectors. We collect images rotated 30° relative to the orientation of the sample components. Otherwise, in the process of skipping lines, we would lose information about the extent of the components especially at the edges.

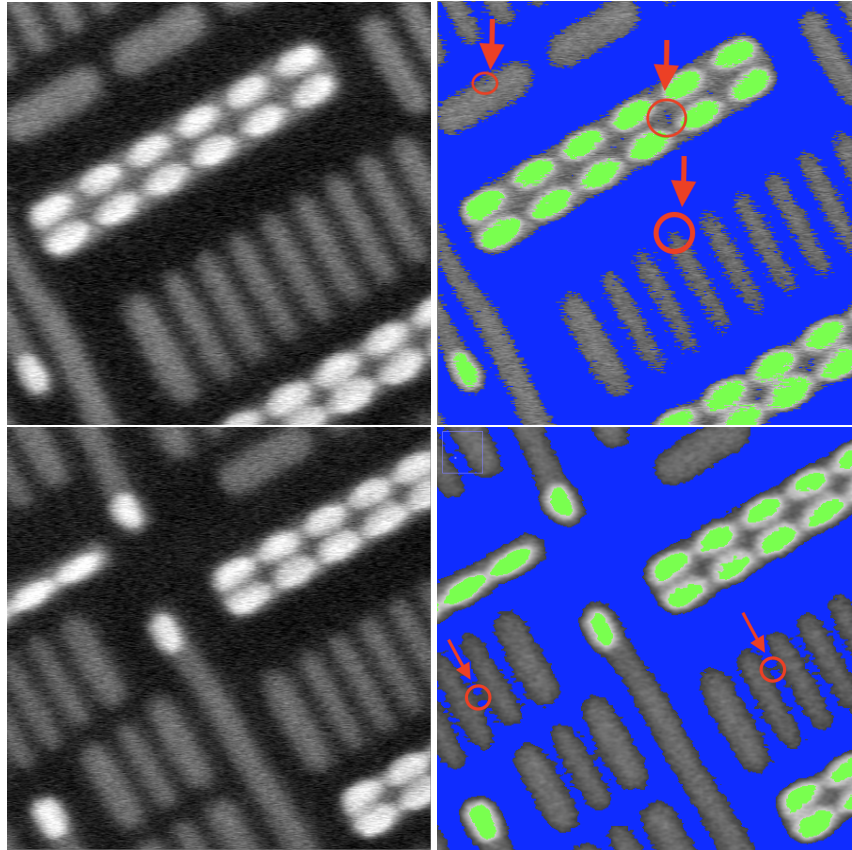


Figure 4.1: *Top*: Segmentation via thresholding. *Bottom*: Thresholding after filtering with a Gaussian filter.

These images have different kinds of noise and signal contrast. Using image fusion we can combine the advantages of the two images, the high contrast of BSE images and the better noise characteristics (i.e., white noise) of the InLens SE images, to reconstruct the complete segmented image. We start with a simple optimization problem, and add complexity in steps.

4.3 Methods

Image Completion Problem

We can reconstruct a complete image from a partial InLens image (Figure 4.5 right) by solving the following optimization problem.

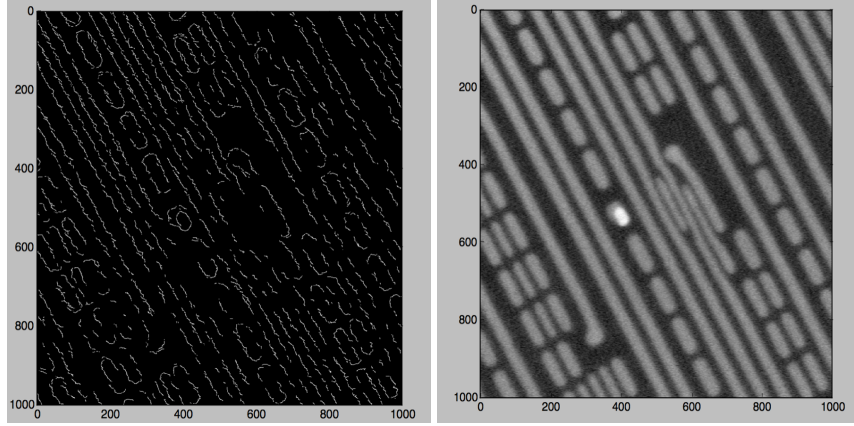


Figure 4.2: Backscattered SEM image and identification of regions for segmentation using Canny Edge detection.

$$\begin{aligned}
 \min \sum_{i \in S, j} \left(V_{i,j} - I_{\text{InLens},i,j} \right)^2 \\
 + \lambda_1 \sum_{i,j} \sum_{(i',j') \in N} W_{i',j'} \left(V_{i+i',j+j'} - V_{i,j} \right)^2,
 \end{aligned} \tag{4.1}$$

where $V_{i,j}$ is the pixel of the reconstructed image at position (i, j) , $I_{\text{InLens},i,j}$ is the corresponding pixel in the (partial) InLens detector image, S is the set of scanned pixel positions, $W_{i',j'}$ is a 2d array of weights for neighbourhood comparisons, and λ_1 is a penalty parameter which determines the trade-off between fitting the data, and the smoothness of the image.

The regularization term, $\sum_{i,j} \sum_{(i',j') \in N} W_{i',j'} \left(V_{i+i',j+j'} - V_{i,j} \right)^2$ penalizes differences between a pixel and its neighbours. We consider neighbours up to a distance of 9, as we show in Figure 4.6. The height of the surface plot is the weight of their difference in value to the central pixel.

In Figure 4.7 right you can see the result of this optimization problem. The resulting images are smooth, with less noticeable noise, but the image quality is not sufficient for segmentation, which is why we introduce image fusion in the next section.

Modelling Rice Noise and Image Fusion

The BSD image has higher contrast, but it has non-white noise as you can see in Figure 4.8 (on the left). The Fourier transform of a line of this noise (in the middle) shows that noise looks like it is low-pass filtered. Close observation of the noise, indicates that it is asymmetric, and personal communication (Phaneuf, 2019) leads us to expect the shape of a decaying exponential. We found that we could approximate this shape by convolving

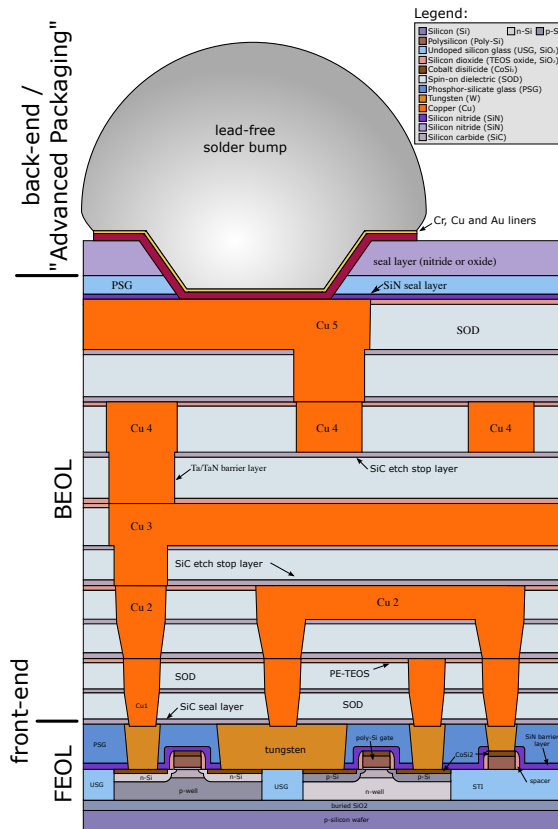


Figure 4.3: The electronic chip with five layers of metallization.¹

¹ This image is licensed under Creative Commons Attribution 2.5 Generic by user Cepheiden at [https://commons.wikimedia.org/wiki/File:Cmos-chip_structure_in_2000s_\(en\).svg](https://commons.wikimedia.org/wiki/File:Cmos-chip_structure_in_2000s_(en).svg)

such a decaying exponential

$$\tilde{\zeta}(x) = \begin{cases} 0 & x \leq 5 \\ e^{-20x+10} & x > 5 \end{cases}$$

with a Gaussian with standard deviation 2, resulting in the shape on the right in Figure 4.8. We call this B . We filter the complete image by convolving with B symbolically $\sum_k B_k V_{i+k,j}$. The difference between this convolution and the BSD image will be noise with the same characteristic, so we convolve the difference to weight the noise by its expected spectrum,

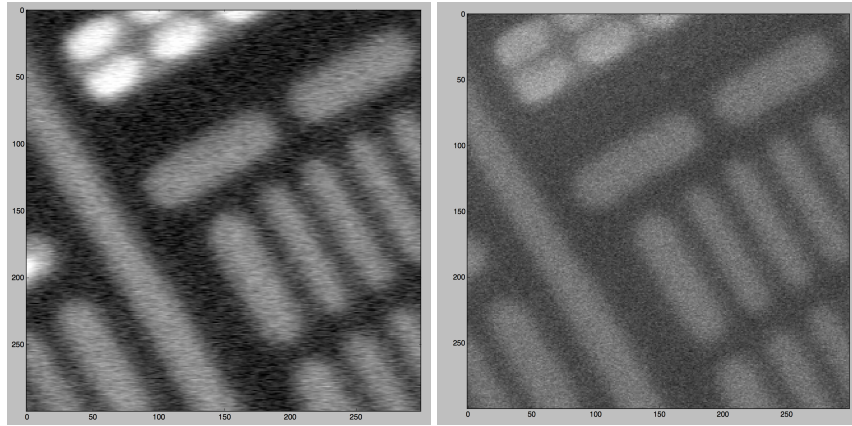


Figure 4.4: *Left*: BSE Detector *Right*: InLens detector SE images of metallization lines

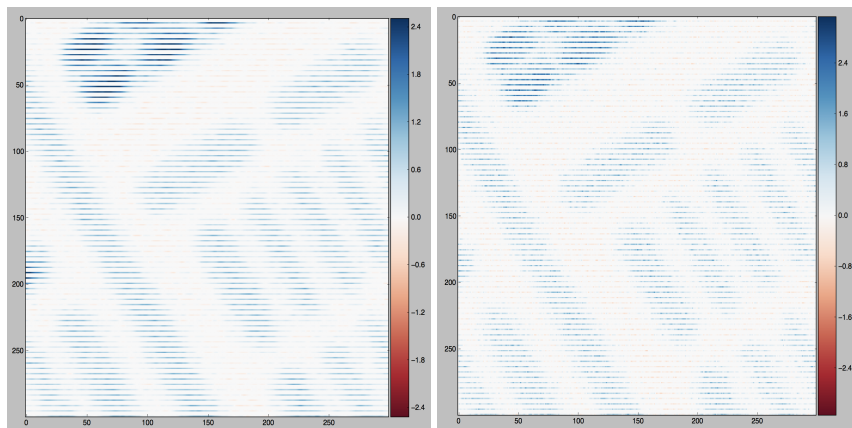


Figure 4.5: Partial BSD and InLens images, showing every fourth scan line.

which could be optimized alone Figure 4.7, but in our case we add to the InLens term, to

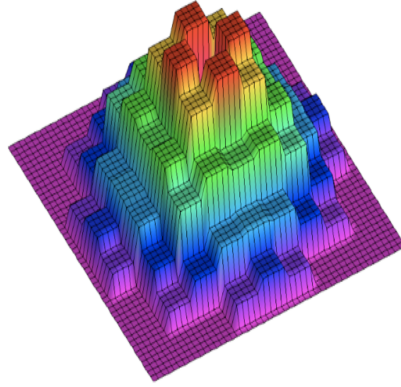


Figure 4.6: Weights of Neighbours.

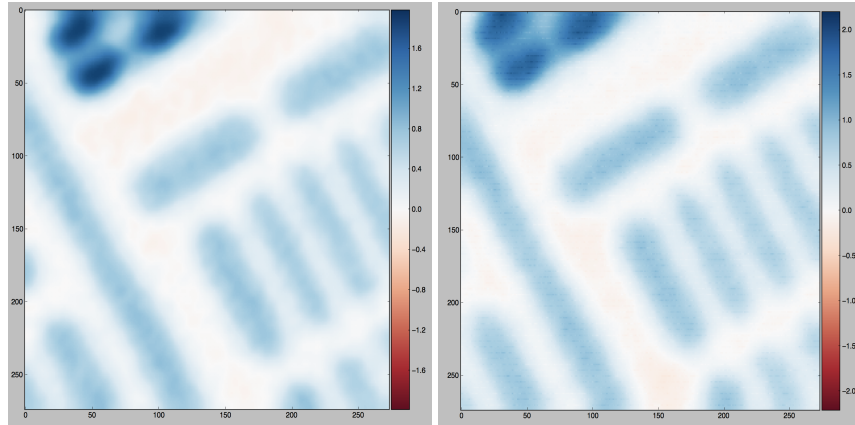


Figure 4.7: *Left*: Results of the first step using only the BSE image, *Right*: Results of the first step using only the InLens image.

create an optimization problem which performs image fusion:

$$\begin{aligned}
 \min \quad & \sum_{i \in \mathcal{S}, j} (V_{i,j} - I_{\text{InLens}, i,j})^2 \\
 & + \sum_{i \in \mathcal{S}, j} \left(\sum_k B_k (I_{\text{BSD}, i,j} - \sum_k B_k V_{i+k,j}) \right)^2 \\
 & + \lambda_1 \sum_{i,j} \sum_{(i',j') \in \mathcal{N}} W_{i',j'} (V_{i+i',j+j'} - V_{i,j})^2.
 \end{aligned} \tag{4.2}$$

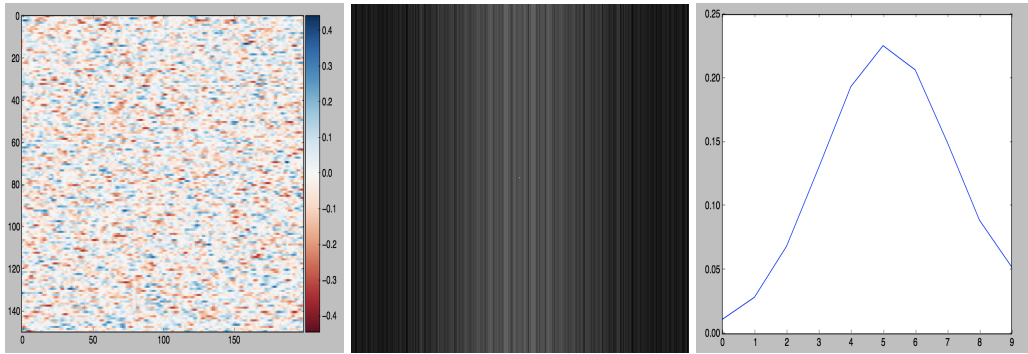


Figure 4.8: *Left*: Sample noise. *Middle*: FFT of a line of noise. *Right*: Empirical point-spread function for noise.

Image Segmentation

Since we want to segment the completed image, we also add a segmentation penalty. Figure 4.9 shows a sixth order polynomial formed by the product of three parabolas. We use this as a penalty because it is the simplest function with three minima. We adjust the minima to correspond to b , d and v , the three grey scale values corresponding to the silicon, buried metallization and vias, although we will see that the the average pixel values are not the values which result in the best segmentation. This penalty is

$$\lambda_2 \sum_{i,j} (V_{i,j} - b)^2 (V_{i,j} - d)^2 (V_{i,j} - v)^2. \quad (4.3)$$

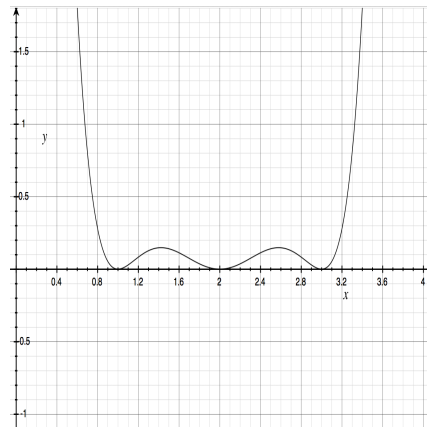


Figure 4.9: minimums in the polynomial.

Non-Linear Optimization Problem

Putting the previous pieces together we obtain an optimization problem which solves the segmentation problem. We solve this optimization problem in two steps. In the first step, we complete the image which serves as an initial guess for the second step which also performs segmentation.

1. First step:

This quadratic problem is insensitive to the initial guess:

$$\begin{aligned}
& \sum_{i \in \mathcal{S}, j} \left(V_{i,j} - I_{\text{InLens},i,j} \right)^2 \\
& + \sum_{i \in \mathcal{S}, j} \left(\sum_k B_k (I_{\text{BSD},i,j} - \sum_k B_k V_{i+k,j}) \right)^2 \\
& + \lambda_1 \sum_{i,j} \sum_{(i',j') \in \mathcal{N}} W_{i',j'} \left(V_{i+i',j+j'} - V_{i,j} \right)^2.
\end{aligned} \tag{4.4}$$

2. Second step:

This non-quadratic, non-convex problem is sensitive to the starting point, so we use the solution to the first problem as a starting point.

$$\begin{aligned}
& \sum_{i \in \mathcal{S}, j} \left(V_{i,j} - I_{\text{InLens},i,j} \right)^2 \\
& + \sum_{i \in \mathcal{S}, j} \left(\sum_k B_k (I_{\text{BSD},i,j} - \sum_k B_k V_{i+k,j}) \right)^2 \\
& + \lambda_1 \sum_{i,j} \sum_{(i',j') \in \mathcal{N}} W_{i',j'} \left(V_{i+i',j+j'} - V_{i,j} \right)^2 \\
& + \lambda_2 \sum_{i,j} \left(V_{i,j} - b \right)^2 \left(V_{i,j} - d \right)^2 \left(V_{i,j} - v \right)^2.
\end{aligned} \tag{4.5}$$

The two parameters λ_1 and λ_2 control the weight of the penalties. By increasing λ_1 the solution will be smoother (blurrier) in the first step, and in the second step all pixels could even be assigned to one segment. Increasing λ_2 increases the attraction to the assigned segment values. If λ_2 is too large, the solution will be a rounded-off version of the initial guess, and the smoothing penalty and fit-to-data term will be ignored.

4.4 Results

We solve this optimization problem in two steps. We normalized the I_{BSD} and I_{InLens} pixel values to be in the range $[0, 2]$. As you can see in Figure 4.10 (on the left) the result of the first step completes the image and the second step segments it (Figure 4.10, right).

In segmenting this kind of data, connectivity is important, but thickness of components is not. In the upper layers of the chip, wires are thicker and there is more space

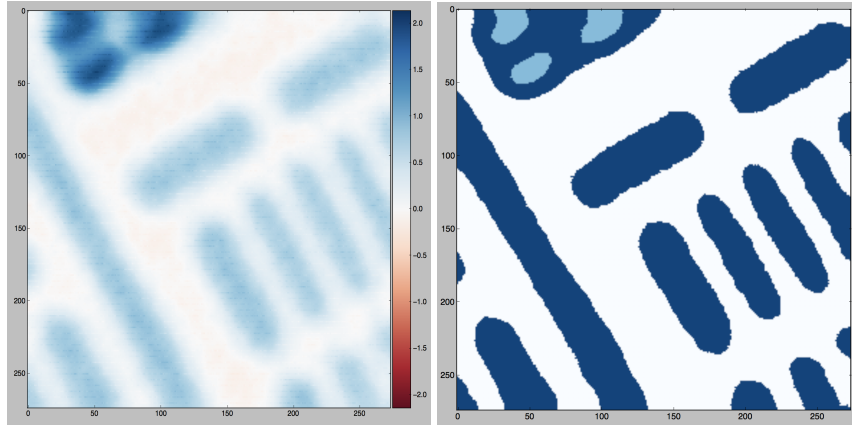


Figure 4.10: *Left*: First step result reconstructed from one fourth of the scan lines, *Right*: Second step result with $b=0$, $d=1$, $v=2$, $\lambda_1=40000$, $\lambda_2=100000$.

between them so it is easier to segment those parts. As we go to lower layers, wires get thinner and more dense. When wires are close enough to each other, the grey level between them never reaches the expected value b , making it harder to segment them. Collecting more lines would help to segment such data. In Figure 4.11 on the left you can see a dense part of the sample. We use just one fourth of the lines. The result of the first step is on the right. With default parameters the result of the second step shows false connection, see Figure 4.12 on the top left. Tuning the parameters to adjust for wire thickness, boundary smoothness, and connectivity, we can find parameters which produce the desired segmentation: Figure 4.12 bottom-right. Comparing the top-right and bottom-right images, we see that the thickness of segmented wires is decreased by increasing the grey value of the background. Comparing the bottom left and bottom-right images, we see that the thickness of the segmented wires is increased by increasing the grey value of the wires, and can be adjusted to completely separate wires.

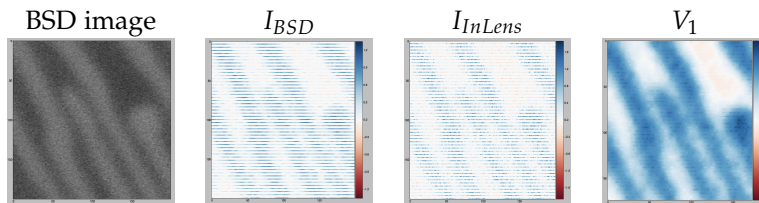


Figure 4.11: *Left*: BSD image, *Middle*: two partial images from BSD and InLens detectors with one quarter of the lines. *Right*: First step result.

In Figure 4.13 we consider the same part of the sample but use twice as much

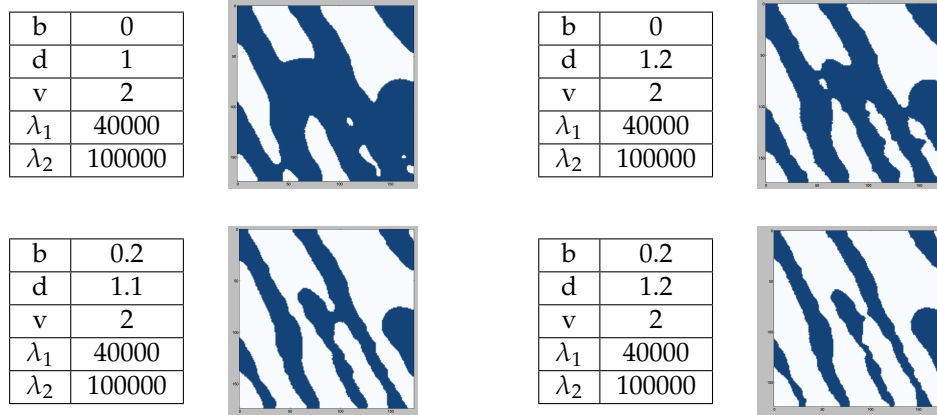


Figure 4.12: Second step results with quarter of scanning lines, and different choices of parameters.

data (every second scan line). We again tune the parameters for the second step obtaining the results in Figure 4.14. Scanning more lines provide us more information so we can generate smoother edges. As shown in the top left image, the default values do not produce the correct segmentation, even with twice as much data. By increasing the grey scale values b and d , we can thin the wires and finally separate them as shown on the image bottom-right. The bottom left image shows how decreasing the penalty variable (λ_2) decreases the connectivity of the sample by decreasing the smoothness.

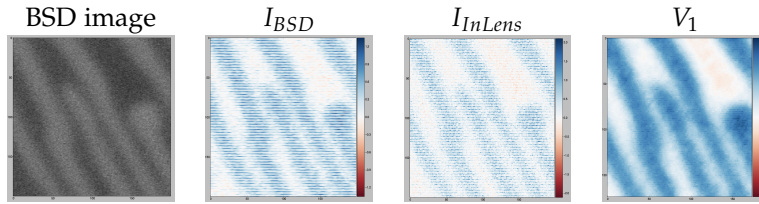


Figure 4.13: *Left*: BSD image, *Middle*: two partial images from BSD and InLens detectors with half of the lines. *Right*: First step result.

4.5 Discussion

In this paper we developed an optimization model which estimates a segmentation based on partial SEM image data. As part of this process, we completed images with only some scan lines acquired. We are able to correctly segment a test image with just one fourth of the lines from the BSD and InLens detectors, which can be collected simultaneously.

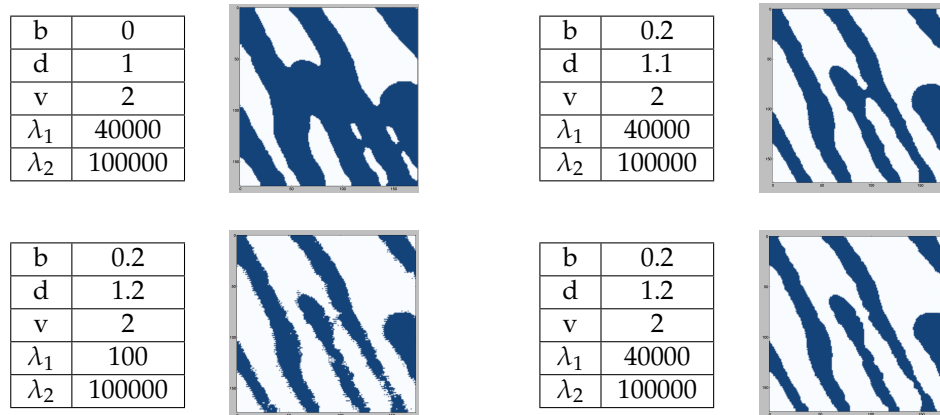


Figure 4.14: Second step results with half the scan lines, and different choices of parameters.

We solve mathematical optimization problems for the two steps in Python 3.5.2 from the Anaconda 4.1.1 distribution running on macOS 10.13.6. Both steps were implemented using Pyomo version 5.5.0 calling Ipopt version 3.12.9.

The first step is a quadratic optimization problem and for a subimage with dimensions 300×300 takes 408.9s in total (36.12s in Ipopt) and the second step is a non-linear optimization problem that takes 642.74s total (229.57s in Ipopt). The way Python generates the optimization problems takes more time than solving them. As future work we will experiment with other solvers to find solutions faster.

4.6 Acknowledgments

We are thankful to the many people at TechInsights for explaining the problem and providing the data and sharing their knowledge with us. We also grateful to Fibics, Inc for explaining the details of detectors physics. We thank NSERC for funding.

Chapter 5

Conclusion

In this thesis we used optimization to extract information from grey-level SEM images. This Thesis has two parts. In the first part we reconstruct three dimensional surfaces from two dimensional SEM images using two modes of the E-T detector (BSE and SE modes). To solve this problem we used two mathematical optimization problems. We made developed both linear and quadratic models. We collect eight BSE-mode images by rotating the stage 45° at a time resulting in four pairs of images collected from opposite directions and consequently having shadows on opposite faces of protrusions. We calculate a heightmap from these opposite image pairs. We also collect eight SE images simultaneously and add those together. The resulting SE image depends on slope but not direction, and we use it to correct steep slopes in the heightmap calculated from the BSE model. We validate the model on a silicon FIB-fabricated sample and we compare the optimization results with AFM tests of the same object. We also test the model on a tin sphere and validated it observing that the results looks like a sphere.

In the second part we reconstruct a segmented image. To save imaging time, we collect just half or even one fourth of scan lines and complete the images afterward. We use image fusion to take advantage of two detectors (capable of scanning simultaneously). Fusing high-contrast BSD images and InLens images with better noise characteristics provide us a complete and segmented image. We use SEM images of semiconductor chips to evaluate the model. These images have three regions and some repetitive patterns. We solve mathematical optimization problems in two steps to both complete the partially scanned images and produce a segmentation.

Bibliography

- ANAND, C.K., TERLAKY, T. & WANG, B. (2004). Rapid, embeddable design method for spiral magnetic resonance image reconstruction resampling kernels, *Optimization and Engineering* **5**, 485–502.
- BAGHAIE, A., TAFTI, A.P., OWEN, H.A., D’SOUZA, R.M. & YU, Z. (2017). Three-dimensional reconstruction of highly complex microscopic samples using scanning electron microscopy and optical flow estimation, *PloS one* **12**, e0175078.
- BEIL, W. & CARLSEN, I. (1991). Surface reconstruction from stereoscopy and “shape from shading” in SEM images, *Machine vision and applications* **4**, 271–285.
- CARLSEN, I. (1985). Reconstruction of true surface-topographies in scanning electron microscopes using backscattered electrons, *Scanning* **7**, 169–177.
- CHEN, D., MIYAMOTO, A. & KANEKO, S. (2012). Robust surface reconstruction in SEM with two BSE detectors, *Mechatronics (MECATRONICS), 2012 9th France-Japan & 7th Europe-Asia Congress on and Research and Education in Mechatronics (REM), 2012 13th Int’l Workshop on*, 64–70, IEEE.
- CZYZYK, J., WISNIEWSKI, T. & WRIGHT, S.J. (1999). Optimization case studies in the neos guide, *SIAM review* **41**, 148–163.
- DESAI, V. & REIMER, L. (1990). Calculation of the signal of backscattered electrons using a diffusion matrix from Monte Carlo calculations, *Scanning* **12**, 1–4.
- DRZAZGA, W., PALUSZYNSKI, J. & SLOWKO, W. (2005). Three-dimensional characterization of microstructures in a SEM, *Measurement Science and Technology* **17**, 28.
- GOLDSTEIN, J.I., NEWBURY, D.E., MICHAEL, J.R., RITCHIE, N.W., SCOTT, J.H.J. & JOY, D.C. (2017). *Scanning electron microscopy and X-ray microanalysis*, Springer.
- HANSEN, P.C. & O’LEARY, D.P. (1993). The use of the L-curve in the regularization of discrete ill-posed problems, *SIAM Journal on Scientific Computing* **14**, 1487–1503.
- KHOLODILOV, O., YA. GRIGORYEV, A. & MYSHKIN, N. (1987). Reconstruction of true topographies of solid surfaces in scanning electron microscopes using secondary electron, *Scanning* **9**, 156–161.
- KRESHUK, A., STRAEHLE, C.N., SOMMER, C., KOETHE, U., CANTONI, M., KNOTT, G. & HAMPRECHT, F.A. (2011). Automated detection and segmentation of synaptic contacts in nearly isotropic serial electron microscopy images, *PloS one* **6**, e24899.

- LEBIEDZIK, J. (1975). Multiple detector method for quantitative determination of microtopography in the SEM, *SCANNING ELECTRON MICROSCOPY/1975 (Part1)* 181–188.
- LEBIEDZIK, J. (1979). An automatic topographical surface reconstruction in the SEM, *Scanning* **2**, 230–237.
- LI, H. & DING, Z. (2005). Monte Carlo simulation of secondary electron and backscattered electron images in scanning electron microscopy for specimen with complex geometric structure, *Scanning* **27**, 254–267.
- MILILLO, T., HARD, R., YATZOR, B., MILLER, M.E. & GARDELLA, J. (2015). Image fusion combining sem and tof-sims images, *Surface and Interface Analysis* **47**, 371–376.
- MIYAMOTO, A., CHEN, D. & KANEKO, S. (2014). Bootstrapping de-shadowing and self-calibration for scanning electron microscope photometric stereo, *Measurement Science and Technology* **25**, 105402.
- MIYAMOTO, A., MATSUSE, H. & KOUTAKI, G. (2017). Robust surface reconstruction by design-guided SEM photometric stereo, *Measurement Science and Technology* **28**, 045405.
- MÜLLER, H.O. (1937). Die Abhängigkeit der Sekundärelektronenemission einiger Metalle vom Einfallswinkel des primären Kathodenstrahls, *Zeitschrift für Physik* **104**, 475–486.
- MULUKUTLA, G.K., GENAREAU, K.D., DURANT, A.J. & PROUSSEVITCH, A.A. (2017). Whole object surface area and volume of partial-view 3D models, *Measurement Science and Technology* **28**, 085003.
- PHANEUF, M. (2019). personal communication.
- SALZER, M., SPETTL, A., STENZEL, O., SMÅTT, J.H., LINDÉN, M., MANKE, I. & SCHMIDT, V. (2012). A two-stage approach to the segmentation of fib-sem images of highly porous materials, *Materials Characterization* **69**, 115–126.
- SHISHIDO, C., TANAKA, M., HAMAMATSU, A. & NAGAO, T. (2011). Improved secondary electron extraction efficiency model for accurate measurement of narrow-space patterns using model-based library matching, *Journal of Micro/Nanolithography, MEMS, and MOEMS* **10**, 043017.
- SIM, K., TSO, C. & TING, H. (2008). Canny optimization technique for electron microscope image colourization, *Journal of microscopy* **232**, 313–334.
- SUGANUMA, T. (1985). Measurement of surface topography using SEM with two secondary electron detectors, *Microscopy* **34**, 328–337.
- TAFTI, A.P., KIRKPATRICK, A.B., ALAVI, Z., OWEN, H.A. & YU, Z. (2015). Recent advances in 3D SEM surface reconstruction, *Micron* **78**, 54–66.
- TAROLLI, J.G., JACKSON, L.M. & WINOGRAD, N. (2014). Improving secondary ion mass spectrometry image quality with image fusion, *Journal of the American Society for Mass Spectrometry* **25**, 2154–2162.
- VROMEN, J. & MCCANE, B. (2009). Red blood cell segmentation from sem images, *2009 24th International Conference Image and Vision Computing New Zealand*, 44–49, IEEE.

- YAN, S., ADEGBULE, A. & KIBBEY, T.C. (2017). A hybrid 3D SEM reconstruction method optimized for complex geologic material surfaces, *Micron* **99**, 26–31.
- YANG, R. & BUENFELD, N. (2001). Binary segmentation of aggregate in sem image analysis of concrete, *Cement and Concrete Research* **31**, 437–441.